

LOCAL ATOMIC ARRANGEMENTS  
AND SOLUTION STRENGTHENING  
OF Ta-Mo AND Ta-Nb ALLOYS

by

Roamer Edward Predmore  
''

Dissertation submitted to the Faculty of the Graduate School  
of the University of Maryland in partial fulfillment  
of the requirements for the degree of  
Doctor of Philosophy, 1975

copy /  
24

(Cap. 2 ENG.)

APPROVAL SHEET

Title of Thesis: Local Atomic Arrangements <sup>AND</sup> ~~Responsible for the~~ Solution  
Strengthening of Ta-Mo and Ta-Nb Alloys

Name of Candidate: Roamer Edward Predmore  
Doctor of Philosophy, 1975

Thesis and Abstract Approved: Richard J. Arsenault  
Richard J. Arsenault  
Professor of Engineering Materials  
Engineering Materials Group, and  
Department of Chemical Engineering

Date Approved: 4/29/75

## ABSTRACT

Title of Dissertation: Local Atomic Arrangements and Solution Strengthening  
of Ta-Mo and Ta-Nb Alloys

Roamer Edward Predmore, Doctor of Philosophy, 1975.

Dissertation directed by: Richard J. Arsenault

Professor

Ta-Nb alloys are shown to form random solid solutions by x-ray diffuse scattering measurements. These alloys have equal size atoms in their pure state with lattice parameters that are invariant in composition, obey Vegard's Law, and exhibit an absence of solid solution hardening and an absence of fracture embrittlement at high solute concentrations. Ta-Mo atoms of about 5% difference in atomic size form short range ordered solid solutions with large atomic displacement effects. The Ta-Mo, and Ta-W, Nb-Mo and Nb-W alloys have in common a lattice parameter that varies in composition with a negative deviation from Vegard's Law. There is also a negative heat of mixing which is well correlated with short range order. In addition, all these alloys show linear solid solution hardening to high solute concentrations at room temperature and fracture embrittlement at high solute concentrations. Diffuse x-ray scattering measurements on Ta-Mo alloys give the short range order parameters and atomic size displacements. The hardening is attributed to a combination of size effect induced substitutional solid solution hardening and short range order induced hardening.

## ACKNOWLEDGMENTS

The author wishes to express his deep appreciation to Professor R. J. Arsenault who suggested the problem and provided guidance and continued encouragement throughout the extended period of this work. Special thanks to Dr. C. J. Sparks, Jr., of Oak Ridge National Laboratory for his encouragement, discussions and assistance with the diffuse x-ray data analysis.

Thanks are given to Professor L. Skolnick for providing the x-ray equipment, to Dr. H. A. Beale for aligning and setting up the x-ray equipment, Dr. Beale again and Dr. G. C. Das, M.I.T., for zone meeting the alloy crystals and Dr. R. D. Deslottes, N.B.S., for the Si single crystal. I wish to thank Mr. L. Kobren, Goddard Space Flight Center, for the electron probe microanalysis of the alloy and Miss J. Jellison, Goddard, for the SEM fractographs. Thanks are given to Dr. J. E. Epperson, Professor R. W. Armstrong and Professor M. J. Marcinkowski for many helpful discussions. I wish to thank Mrs. Kay Alexander for typing the dissertation.

This author gratefully acknowledges the support of Dr. H. E. Frankel, Professor H. W. Price and Mr. C. L. Staugaitis of Goddard. This research was sponsored by the Advanced Research Projects Agency and Administered through the Center of Materials Research at the University.

Finally the author wishes to express his appreciation to his wife, Renetta, for her never ending devotion and encouragement.

TABLE OF CONTENTS

Chapter	Page
ACKNOWLEDGMENTS . . . . .	ii
LIST OF TABLES . . . . .	v
LIST OF FIGURES . . . . .	vi
I. BACKGROUND . . . . .	1
A. Introduction . . . . .	1
B. Lattice Parameter . . . . .	1
C. Substitutional Solid Solution Hardening . . . . .	2
D. Thermodynamic Properties . . . . .	5
II. EXPERIMENTAL PROCEDURE . . . . .	6
A. Zone Melting and Crystal Growth . . . . .	6
B. Sample Preparation . . . . .	7
C. X-Ray Diffraction Techniques . . . . .	9
III. X-RAY DIFFRACTION THEORY . . . . .	14
IV. EXPERIMENTAL RESULTS AND DISCUSSIONS . . . . .	19
A. Microscopic Fracture Processes . . . . .	19
B. Lattice Parameter of Ta-Mo Alloys . . . . .	21
C. Diffracted Intensity from Ta-Mo Alloys Along the $h_1, 00$ Axis . . . . .	21
D. Diffuse X-Ray Scattering from the $h_1 h_2 0$ Plane of Reciprocal Space from Ta, Mo and Ta-Nb Alloy . . . . .	22
E. Scattering from the $h_1 h_2 0$ Plane of Reciprocal Space from Ta-Mo Alloys . . . . .	24
F. Short Range Order in the Mo-37 at.% Ta and Mo-21 at.% Ta . . . . .	26

TABLE OF CONTENTS - Continued

Chapter	Page
G. Atomic Displacement Effect for Mo-Ta Alloys . . . . .	28
H. Substitutional Solid Solution Hardening and Short Range Order Hardening . . . . .	33
I. Suggestions for Future Research . . . . .	35
V. CONCLUSIONS . . . . .	
REFERENCES . . . . .	66
LIST OF SYMBOLS . . . . .	71

LIST OF TABLES

Table	Page
I. Zone Melting and Crystal Growth Conditions . . . . .	40
II. Diffuse X-Ray Measurement Conditions . . . . .	43
III. Two Dimensional Short-Range Order Parameters $A_{\ell m}$ For the Mo-21 and Mo-37 at .% Ta Alloys . . . . .	44
IV. Atomic Displacement Coefficients $\Gamma_{\ell m}^m$ For Mo-37 at .% Ta . . . . .	45
V. Atomic Displacement Coefficients $\Gamma_{\ell m}^m$ For Mo-21 at .% Ta . . . . .	46
VI. Observed and Calculated Short-Range Order Parameters $A_{\ell m}$ for the Mo-21 and Mo-37 at .% Ta Alloys . . . . .	47
VII. Elastic Strain Terms $L_{111}$ Derived from X-Ray Measure- ments of Atomic Displacements Compared to Those Calculated from Lattice Constants Assuming Hard Spheres . . . . .	48

LIST OF FIGURES

Figure	Page
1 BCC Substitution Solid Solution Hardening of Ta and Nb at 300 K . . . . .	49
2 DPH Hardness of Binary Refractory Alloys at 300 K . . . . .	50
3 DPH Hardness of Binary Refractory Alloys at 300 K . . . . .	51
4 Schematic Representation of the Diffuse Scattering Geometry . . . . .	52
5 Geometry of the Three-Circle Single-Crystal Diffractometer . . . . .	53
6 The Method of Scanning the Elementary Volume . . . . .	54
7 Fractographs of Refractory Binary Alloys at 300 K . . . . .	55
8 Lattice Parameters of Ta-Mo Alloys. Straight line is a plot of Vegard's Law . . . . .	56
9 Diffracted Intensity Along $(h_1, 0, 0)$ Axis in Reciprocal Space for Ta-Mo Alloys, Illustrating Asymmetry of the Short Range Order Peaks about (100) and (300) Positions . . . . .	57
10 Diffracted X-Ray Intensity Distribution in the $h_1 h_2 0$ Plane of Reciprocal Space for Mo at Ambient Temperature. Counts per 30 sec . . . . .	58
11 Diffracted X-Ray Intensity Distribution in the $h_1 h_2 0$ Plane of Reciprocal Space for Ta at Ambient Temperature. Counts per 30 sec . . . . .	59
12 Diffracted X-Ray Distribution in the $h_1 h_2 0$ Plane of Reciprocal Space for Nb-22% Ta at Ambient Temperature. X-Ray Intensity in Counts per 30 sec . . . . .	60
13 Diffracted X-Ray Intensity Distribution in the $h_1 h_2 0$ Plane of Reciprocal Space for Mo-91% Ta at Ambient Temperature. X-Ray Intensity in Counts per 30 sec . . . . .	61

LIST OF FIGURES - Continued

Figure	Page
14 Diffuse Intensity Distribution in the $h_1 h_2 0$ Plane of Reciprocal Space for Mo-37% Ta at Ambient Temperature. Diffuse X-Ray Intensity in Counts per 60 sec . . . . .	62
15 Diffuse Intensity Distribution in the $h_1 h_2 0$ Plane of Reciprocal Space for Mo-21 a/o Ta at Ambient Temperature. Diffuse X-Ray Intensity in Counts per 60 sec . . . . .	63
16 Model for the Short Range Ordered Structure of Mo-37 at .% Ta . . . . .	64
17 Model for the Short Range Ordered Structure of Mo-21 at .% Ta . . . . .	65

CHAPTER I

BACKGROUND

A. Introduction

Binary refractory alloys of Nb, Mo, Ta and W form a continuous series of BCC solid solutions. These binary solid solutions exhibit two types of mechanical properties; alloys of elements with essentially the same atomic size in the pure state (0.01Å or about 0.3% difference), Ta-Nb and Mo-W, show almost no substitutional solid solution hardening; whereas the pairs of elements Nb-Mo, Nb-W, Ta-Mo and Ta-W have about a 5% difference in atomic size and exhibit substitutional solid solution hardening. The purpose of this investigation was to measure the local-order and displacements of atoms in binary alloys of each type using the diffuse x-ray scattering technique of Cowley,<sup>(1)</sup> and Warren, Averbach and Roberts<sup>(2)</sup> and to relate this local atomic structure to the observed mechanical properties.

B. Lattice Parameter

The Ta-Nb and Mo-W alloys have very small differences in their atomic size, whereas the other binary combinations have about a 5% atomic size difference. The lattice parameter of the alloys of Ta-Nb and Mo-W are found invariant with composition in agreement with Vegard's Law when measured by Williams and Pechin<sup>(3)</sup> and Buckle,<sup>(4)</sup> respectively. However, the binary alloys formed from atoms of different sizes, Ta-Mo, Ta-W, Nb-Mo and Nb-W, were found to have a negative deviation from Vegard's Law<sup>(5,6,7,8,9)</sup> which indicates a preference for unlike nearest neighbors.

### C. Substitutional Solid Solution Hardening

The solute addition can affect both the thermal component of the yield stress (effective stress  $\tau^*$ ) and the athermal component (temperature independent stress  $\tau_\mu$ ) in BCC alloys of different sized atoms. (10, 11, 12, 13, 14) The temperature at which  $\tau^*$  is zero is defined as  $T_c$ . Above  $T_c$  the yield of flow stress consists of the temperature independent component  $\tau_\mu$ .  $T_c$  is slightly above ambient temperature for these alloys. (10) Though room temperature measurements are slightly below the plateau temperature determined by Rudolph and Mordike (10) and others (11, 12) on these BCC alloys, their data show that the change in the shear stress for varying compositions of the same alloying elements is almost temperature insensitive above 300°C. The change in our hardness measurements made at room temperature are predominantly sensitive to the solid solution hardening components of the athermal stress. Our measurements extend the compositions measured by the previous authors to cover the entire compositional range.

An earlier work (10) on Ta-Nb was interpreted as showing that the lack of strengthening and of size difference in the pure state for Ta and Nb, even though their elastic moduli differed by  $11 \times 10^6$  psi, precluded an interpretation that solution strengthening was mostly dependent on their shear moduli. This conclusion has also been reached by others (10, 11, 12, 13, 14, 15) and differs with the FCC solution strengthening interpretation put forth by Fleischer (16) and the BCC solution strengthening interpretation put forth by Suzuki (17) and Boser (18) which are predominantly based on the modulus difference.

The absence of substitutional solid solution hardening at ambient temperature was observed for Nb-Ta. (10, 12) The linear substitutional solid solution hardening was observed for Nb-W, (19) for Nb-Mo (11, 20) and for Ta-W. (21, 22) The above observations were made on tantalum or niobium rich alloys because of their room temperature ductility. Figure 1 shows the linear solution hardening for the Ta and Nb rich alloys at 300 K. The Ta-Nb alloys with the same atomic size show no substitutional solid solution hardening. The alloys with about 5% difference in atomic size, Ta-Mo, Ta-W and Nb-Mo, show the same linear solution hardening (Fig. 1). Small changes in the slope of the linear solution hardening data as reported in the literature can be caused by either varying interstitial concentrations, differences between compression and tensile testing or crystal orientation. The observation of an absence of hardening in Ta-Nb and Mo-W alloys composed of atoms of the same atomic size but different shear moduli and the large solution hardening in alloys with about 5% atomic size difference indicates that atomic size effect and/or short range order may be the more predominant cause of hardening.

The inherent brittle fracture characteristics of Mo rich and W rich binary alloys make it very difficult to perform tensile or compressions tests to measure solid solution hardening. Thus diamond pyramid hardness tests were utilized where yield strength data was not available. The diamond pyramid hardness values for the binary alloys at ambient temperature are plotted in Figures 2 and 3. The DPH values measured by the authors were obtained using a 100 gram load. The Mo-W hardness values fit the same hardness curve. (23, 24) The hardness values for the Nb-Ta alloys fit on a line joining Ta and Nb which is



similar in behavior to the yield strengths. Both the Nb-Ta and Mo-W alloys formed from elements of the same atomic size show little increase in hardness upon alloying.

The Mo-Ta hardness values shown in Figure 2 are in good agreement with the other measured values.<sup>(23)</sup> The DPH hardness variation with solute concentration for Nb-W, Nb-Mo and Ta-W are plotted in Figure 3. The data for arc cast Nb-W alloys are from Braun et al.<sup>(25)</sup> and show a small increase in hardness above the zone refined Nb-W alloys because of larger interstitial concentration. The Ta-W hardness values were reported by Meyers,<sup>(24)</sup> Westgren et al.<sup>(26)</sup> and Kieffer et al.<sup>(27)</sup> The hardness values agree well and show a relation similar to the Nb-W alloys. The Nb-Mo hardness values in Figure 3 were reported by Semchysen et al.<sup>(23)</sup> and Braun et al.<sup>(25)</sup> The Ta-Mo, Ta-W, Nb-Mo and Nb-W BCC substitutional solid solution alloys with about a 5% atomic size difference show a large increase in hardness with solute concentration. When the Mo and W atoms are dissolved in the Ta and Nb solid, they produce the same linear solution hardening rate of  $1.7 \text{ kg/mm}^2$  per atomic percent solute (Fig. 1) and a linear hardness increase (Figs. 2, 3) of 11 DPH numbers per atomic percent solute.

Dugdale<sup>(70)</sup> and Tabor<sup>(71)</sup> have shown the DPH values to be about three times the flow stress of polycrystalline alloys. The flow stress is normally 2.5 times the yield stress. The yield stress is twice the critical resolved shear stress for a crystal orientation factor of two. Thus the DPH value is expected to be about 15 times the critical resolved shear stress. For tantalum the ratio of hardness to critical resolved shear stress is 25 at 300K. Using the range of proportional limits or critical resolved shear stress values from Arsenault et. al.,<sup>(72)</sup> the DPH to critical resolved shear stress range from 11 to 36. The ratio of DPH to critical resolved shear stress for Ta is about the same as Mo and within a factor of two of the expected ratio of 15. The subgrain size was found to be independent of composition for the Mo rich Ta alloys with the subgrain diameter of Mo-21 at.

% Ta ( $2.2 \times 10^{-3}$  mm) being about equal to the subgrain diameter of Mo-37 at. % Ta ( $3.6 \times 10^{-3}$  mm). The diamond pyramid micro hardness of the Mo-21 at. % Ta alloy subgrain boundaries taken with a 5 gram load on a Reichert Metallograph showed no evidence of subgrain boundary hardening. Subgrain boundary hardening discussed by Armstrong<sup>(73)</sup> is therefore expected to have only limited influence on the rate of alloy hardening in Ta-Mo alloys. The linear variation of DPH with alloy content for Mo-Ta alloys is therefore attributed to solution hardening plus short range order because the hardness values are the same for arc cast alloys as zone melted alloys, the subgrain size is about the same for the Mo rich alloys and the DPH to critical resolved shear stress ratio agrees approximately with the expected value. The linear solid solution plus short range order hardening for Mo rich Ta alloys is calculated to be  $1.2 \text{ Kg/mm}^2$  using the ratio of DPH to critical resolved shear stress for Ta rich Mo and the 8 DPH per atomic percent Ta value.

#### D. Thermodynamic Properties

The thermodynamic properties of Ta-Mo, Ta-W and Nb-Mo alloys at high temperature were measured by Singhal and Worrell.<sup>(28,29)</sup> Large negative heats of mixing and the negative deviation from Vegard's Law for the lattice parameters normally associated with ~~short~~<sup>SRO</sup> range order were observed. The primary cause of the negative heat of mixing is attributed primarily to electronic interaction and size interaction to a limited extent. These interactions cannot be separated. The negative excess entropies of mixing were used to calculate short range order parameters of -0.23, -0.20 and -0.14 for Ta-Mo<sup>Nb-Mo</sup> and Ta-W respectively using the quasi-chemical theory by Averbach.<sup>(77)</sup>

## CHAPTER II

## EXPERIMENTAL PROCEDURE

A. Zone Melting and Crystal Growth

Alloy single crystals and polycrystals were formed by zone melting. A summary of the melting conditions and resulting alloys are shown in Table I. The zone melting apparatus and procedure have been described.<sup>(30)</sup> The materials used to make up rod type charges for the zone melter were 1.6 mm diameter Ta wire (99.9 wt .% or greater Ta) supplied by Fansteel, 9.5 mm diameter arc melted Nb rods (99.9 wt .% or greater Nb) supplied by Wah Chang, 9.5 mm diameter Ta rods (99.999 wt .% Ta) supplied by Materials Research Corp. and 6.3 mm diameter arc cast Mo rods (99.97 wt .% Mo) supplied by Climax Molybdenum. The Mo and Ta single crystals were grown by passing either one or two molten zone passes along the rod charge length to purify the Ta and Mo followed by a zone pass at minimum speed (3.0-3.5 mm/min) to grow single crystals. The minimum pressure in the zone melter and the minimum zone speed during melting are reported in Table I. The Mo rich Ta alloy single and polycrystal samples were grown from rod charges. The Mo rods were slotted by machining, cleaned in acetone several times. Ta wires were then peened into the slots. The Ta-Mo rod charges were welded and degassed at higher zone speeds than single crystals were grown at minimum zone speeds (2.7 to 3.5 mm/min) as reported in Table I. The Ta rich Mo alloys were prepared from a Ta rod filled with Mo wires. The rods were zone melted to purify and degas the samples before single crystals were grown at 3 mm/min. The Mo-W alloys were melted from a Mo rod containing three 1.6 mm diameter W wires peened

into slots. The grain size increased with slower zone speed but even the minimum zone speed of 1.2 mm/min produced an equiaxed polycrystalline structure. A relatively greater evaporation due to the high vapor pressure of Mo was observed for Mo-Ta and Mo-W alloys. Concentrated Nb-W alloys were also polycrystalline at the lowest zone speed of 2.5 to 3.5 mm/min. The preferential evaporation of Nb was expected but not observed. The Ta-Nb polycrystal and single crystal samples were grown from a slotted Nb rod filled with Ta wires. A preferential evaporation of Nb was observed.

B. Sample Preparation

The single crystals for diffuse x-ray diffraction samples were identified within the zone melted rods by a series of Polaroid Laue photographs taken normal to the axis of the rod. A vise featuring rotation about three axes was mounted on a Norelco x-ray machine to hold the samples in the x-ray beam. The plane of the vise and the plane of the XR-7 Polaroid Laue Camera were positioned normal to the x-ray beam. The zone melted rod and its supporting bar were mounted in the vise with their axis normal to the x-ray beam. Laue photographs were taken at each centimeter interval along the length of the zone melted rod as it was translated normal to the copper x-ray beam. A series of identical Laue patterns of the same orientation enabled the identification of a single crystal. Laue photographs of several zone melted rods produced either rings or spots because of residual surface effects from zone melting. The surface metal was removed by a solution of 10 cc. HF, 10 cc. HNO<sub>3</sub> and 30 cc. lactic acid, or a solution of 30 cc. HCl, 30 cc. HF and 15 cc. HNO<sub>3</sub> or by electropolishing in 90 cc. H<sub>2</sub>SO<sub>4</sub> and 10 cc. HF. The Laue photographic procedure was repeated to identify the single crystals.

The single crystals were cut out of the zone melted rods for x-ray diffraction samples. The remainder of the rod was used for hardness samples, fracture samples and electron probe microanalysis. The single crystals were mounted on a 2.5 cm by 0.64 cm by 5 cm steel plate with small pieces of Plasticine. The steel plate was mounted in the vise for Laue pictures. By repositioning the sample on the plate and taking Laue photographs at each position, the (100) or (110) plane was oriented normal to the copper x-ray beam and parallel with the edge of the plate. The sample was bonded to the steel plate with Hysol epoxy adhesive. The plate was mounted on a magnetic chuck and sectioned in a plane parallel to the edge of the plate with a Micro-matic Precision Wafering machine using an alumina (XA 1803-P-RR5) cut off wheel supplied by Allison-Campbell. The x-ray samples were then chipped off the steel plate. The (100) or (110) cut surface of the sample was placed face down in a 3.2 cm diameter mounting die, surrounded by a 301 stainless steel ring and mounted in glass filled diallyl phthalate. The stainless steel ring kept the mount flat during grinding. The sample was wet ground on 240-, 400-, and 600-grit SiC abrasive paper. It was mechanically polished with 0.3 micron alumina in a 20% chromic acid water solution, 0.055 micron alumina in a 20% chromic acid and water solution then chemically polished in a solution of 10 cc. HF, 10 cc. HNO<sub>3</sub> and 30 cc. lactic acid to remove the deformed surface metal. Clear, small Laue spots were taken to indicate an absence of deformed surface metal. Both a crystal of (100) and (110) orientation was cut for each composition.

The samples for hardness testing were cut from zone melted alloy rods using a metal cut-off wheel and water as a coolant. The samples were mounted

in glass fiber filled, AB diallyl phthalate supplied by Buehler using a heated piston-cylindrical die under pressure. The samples were ground by hand using 180-, 240-, 400- and 600-grit SiC abrasive papers covered with water. The samples were polished on a wheel covered with Buehler Miracloth using a slurry of 15 g fine alumina, 35 cc. H<sub>2</sub>O and 5 cc. of 20 percent chromic acid. DPH measurements were then taken using a 100 gram load. The DPH values are reported in Figures 1 and 2. The details of metallographic preparation are reported in DMIC Memorandum 37.<sup>(31)</sup>

The samples for electron probe microanalysis were cut from the zone melted rods and mounted in glass filled diallyl phthalate (2.54 cm diameter). Each sample was polished on a new sheet of 180-, 240-, 400- and 600-grit SiC abrasive paper to avoid contamination. The chemical composition was measured by electron probe microanalysis at five or more points on each sample and corrected for absorption effects.<sup>(32)</sup>

The fracture surfaces of Ta, Nb and Ta-Nb alloys were obtained by tensile loading rod samples in an Instron tensile machine until fracture. The cleavage fracture surfaces were prepared by clamping the zone melted samples in a vise and impacting them with a hammer. The fracture surfaces were viewed and photographed with an Ultrascan scanning electron microscope.

### C. X-Ray Diffraction Techniques

The x-ray measurements were made using CuK radiation monochromated by diffraction from a double bent LiF crystal similar to Warren,<sup>(33)</sup> Cowley<sup>(1)</sup> and Borie and Sparks.<sup>(34)</sup> A General Electric XRD-6 x-ray generator and power supply formed the basis of the instrument used for these measurements. The

G. E. CA8-L copper tube was inserted into a table mounted adjustable horizontal tube support. The temperature of the water cooled tube was controlled with a G. E. SPG-4 heat exchanger. The line voltage was stabilized with a G. E. line voltage regulator. Figure 4 shows the arrangement of the x-ray source, the monochromator crystal, sample and detector. The doubly bent LiF monochromator  $\text{CuK}_\alpha$  radiation was supplied by Electronics and Alloys, Inc. The monochromator crystal was based on a design by Warren,<sup>(33)</sup> and the fabrication techniques of Chipman,<sup>(35)</sup> Sparks and Borie<sup>(36)</sup> and Schwartz, Morrison and Cohen.<sup>(37)</sup> The doubly bent LiF monochromator crystal was supported and aligned using an Electronics and Alloys primary beam monochromator. The sample was supported by the Electronics and Alloys adjustable flat sample holder in the General Electric Single Crystal Orienter which was in turn mounted on the General Electric SPG-2 x-ray spectrogoniometer. The diffracted x-ray beam intensity was measured with an Argon filled proportional counter (G. E. SPG-8) with a low noise preamplifier. The parasitic air scattering was reduced by introducing 1.2 cm diameter lead tubes extending from the receiver slits and from the monochromator to within 4 cm of the crystal center. In addition a knife edge was mounted 1 mm from the crystal and positioned normal to the crystal plane and the plane of the incident and diffracted beam. The detector bias potential ( $\pm 0.02\%$ ) was provided by a model 312A Baird Atomic Super Stable high voltage power supply. The Argon detector preamplifier (Ortec 109PC) utilized a field effect transistor for low noise amplification of the detector signal. The amplifier (Ortec 485) was set so the peak of the pulse distribution was at a 5 volts on the 0 to 10 volt scale of the single channel analyzer (Ortec 406A). The lower

limit of the discriminator was set at 2.5 volts to eliminate low energy noise and the upper limit was set at 7.5 volts to eliminate the  $\frac{\lambda}{2}$  component of the x-ray beam. Diffuse x-ray measurements of the Ta and Mo single crystals showed no evidence of the  $\text{CuK}_\alpha \frac{\lambda}{2}$  peak. The signal was then sent to a digital ratemeter (Ortec 434). The output from the digital ratemeter was then sent through a print out control to a 33C Teletype printer or to a G. E. model 8 HF strip chart recorder.

The x-ray equipment was aligned following the procedures described in great detail by Schwartz, Morrison and Cohen<sup>(37)</sup> and Gilmore.<sup>(38)</sup> The x-ray beam from the monochromator passed over the center of rotation of the goniometer and into the detector through a receiving slit of  $2\theta = 0.02^\circ$ . A glass slide was placed in the flat sample holder for alignment. With  $\chi = 0^\circ$ , the slide was moved into the x-ray beam utilizing the y motion to intersect half the beam intensity (Fig. 5). Clockwise and counter clockwise adjustments of the  $\omega$  angle positioned the slide and flat sample holder parallel to the x-ray beam by achieving maximum intensity. The glass slide was rotated  $\theta = 180^\circ$  and the goniometer including the flat sample holder were moved along the y axis to again obtain half the incident beam intensity. The glass slide was positioned in the vertical center of the beam by the procedure of rotating  $\chi$  by  $90^\circ$ , blocking half the beam at both  $\varphi = 0^\circ$  and  $180^\circ$  and by adjusting the height of the goniometer and the monochromator.

The alignment of the equipment was checked by measuring the lattice parameters of a high purity Si single crystal from the National Bureau of Standards as well as zone melted Ta and Mo single crystals. The crystals were placed in the flat sample holder. The goniometer was rotated to the  $2\theta$  angle for the Bragg peaks. The  $\varphi$ ,  $2\theta$  and  $\chi$  angles were adjusted to find the maximum Bragg peak

intensity for the  $\text{CuK}_\alpha$  radiation. The  $2\theta$  angles measured at the  $\frac{3}{4}$  maximum peak height of each peak were recorded and averaged. The resulting lattice parameters of Si, Mo and Ta were found to be 5.428Å, 3.147Å and 3.303Å, respectively. The agreement with the reported value of Si of 5.430Å by Schwartz, Morrison and Cohen<sup>(37)</sup> and the values of 3.147Å for Mo and 3.303Å for Ta from the ASM Handbook<sup>(39)</sup> demonstrated accurate equipment alignment.

The  $h_1 h_2 0$  planes in the single crystals were aligned with respect to incident beam and the detector by adjusting  $\chi$ ,  $\varphi$ ,  $\omega$ , X and Y to obtain the maximum intensity from the 110, 220 and 200 Bragg peaks at their respective  $2\theta$  angles with  $\chi$  set at  $0^\circ$  or  $45^\circ$ . The crystal was translated in the plane of the flat sample holder to intercept the total incident beam as determined by using a small fluorescent screen. The detector was set on the 200 or 220 Bragg peak for a crystal face cut parallel to the 100 or 110 face respectively while the intensity was continuously monitored. A knife edge air scattering shield similar to that described by Rudman,<sup>(40)</sup> was positioned normal to and within 1 mm of the crystal face without reducing the counting rate on the detector. The data was collected between  $2\theta = 15^\circ$  and  $2\theta = 60^\circ$  in equally spaced  $1^\circ$  to  $3^\circ$  steps. The knife edge was removed at high  $2\theta$  angles without an increase in the parasitic air scattering. The stepwise scan was continued from  $2\theta = 60^\circ$  to  $2\theta = 140^\circ$ . The scan was repeated for equally spaced  $1^\circ$  to  $5^\circ$  increments of  $\chi$  ranging from  $0^\circ$  to  $45^\circ$  to map the diffuse x-ray scattering in the  $h_1 h_2 0$  plane (Fig. 6). In order to measure the incident beam power, using the method of Warren and Averbach,<sup>(56)</sup> a polystyrene was inserted in the sample holder,  $\chi$  was set at  $0^\circ$ ,  $\omega$  was set at  $0^\circ$  and diffracted intensity was counted at  $2\theta = 100^\circ$ . Table II lists the detector slit,

x-ray tube power and diffracted intensity for polystyrene measured at  $2\theta = 100^\circ$  for the measurements along the  $h_1 00$  line and in the  $h_1 h_2 0$  plane in reciprocal space. The 100 and 110 crystallographic planes were not exactly coplanar with the cut surface of the sample introducing an absorption error. The crystals were rotated  $\varphi = 180^\circ$  and the diffuse intensity was remeasured near the LRO positions. The diffuse intensity for  $\varphi = 0^\circ$  and  $\varphi = 180^\circ$  were averaged to correct for absorption.

Measurement of the short range order and atomic displacement terms using powder samples or one dimensional data was considered in order to reduce the time required to collect and reduce the data. Walker and Keating<sup>(76)</sup> made measurements along more than one direction in reciprocal space and concluded that neither two or three dimensional short range order terms nor the atomic displacement terms could be recovered with sufficient accuracy to describe the short range order structure in the alloy. In the case of powder samples, the detailed structure of the diffuse intensity distribution is lost because of the averaging of the intensity over a spherical shell about the origin, and a precise interpretation in terms of the order and atomic-displacement parameters is not possible.<sup>(36)</sup> Therefore it was necessary to collect and reduce two dimensional data to obtain an accurate measurement of the short range ordered structure.

## CHAPTER III

## X-RAY DIFFRACTION THEORY

The total measured intensity is the sum of the following contributions:

$I_{\text{ORDER+AD}}$ , the modulated Laue monotonic intensity we seek to recover;  $I_{\text{F+S}}$ , the fluorescence from the sample and diffraction by objects other than the sample;  $I_{\text{C}}$ , Compton or incoherent scattering from the sample;  $I_{\text{TDS}}$ , temperature-diffuse scattering from the sample;  $I_{\text{FUND}}$ , sharp fundamental Bragg reflections; and  $I_{\text{H}}$ , Huang diffuse intensity. According to kinematic diffraction theory, the total coherently scattered x-ray intensity,  $I_{\text{cu}}$ , at a given position in reciprocal space is given in electron units as

$$I_{\text{cu}} = \sum_p \sum_q f_p f_q e^{i\mathbf{K} \cdot \mathbf{R}_{pq}} \quad (1)$$

where  $f_p$  and  $f_q$  are the scattering factors of the atoms situated at sites  $p$  and  $q$ ,  $\mathbf{K}$  is  $2\pi$  times the diffraction vector, and  $\mathbf{R}_{pq}$  is the interatomic vector. According to Warren, et al.<sup>(2)</sup> it is conventional to consider the coherently scattered intensity from binary solid solutions as divided into two parts:  $I_{\text{FUND}}$  which is independent of the state of order and which gives rise to the sharp fundamental Bragg reflections, and  $I_2$ , which depends on how the atoms are arranged on the atomic sites. A quadratic approximation to the displacements of the atoms off the average lattice sites, according to Borie and Sparks<sup>(41)</sup> gives the diffuse intensity associated with the atomic order and atomic displacements ( $I_{\text{ORDER+AD}}$ ), Huang diffuse ( $I_{\text{H}}$ ) and first order temperature diffuse scattering ( $I_{\text{TDS}}$ ). The result specialized for the  $h_1 h_2 0$  plane for body or face-centered cubic binary

alloys, can be expressed as

$$\begin{aligned} I(h_1, h_2, 0) = & NX_A X_B (f_A - f_B)^2 \sum_{\ell} \sum_m \sum_n \alpha_{\ell mn} \cos 2\pi h_1 \ell \cos 2\pi h_2 m \\ & - NX_A X_B (f_A - f_B)^2 \sum_{\ell} \sum_m \sum_n [h_1 \gamma_{\ell mn}^{\ell} \sin 2\pi h_1 \ell \\ & \cos 2\pi h_2 m + h_2 \gamma_{\ell mn}^m \cos 2\pi h_1 \ell \sin 2\pi h_2 m] \\ & - 4\pi^2 N \sum_{\ell} \sum_m \sum_n [h_1^2 \langle \delta^2 \rangle_{\ell mn}^{\ell} + h_2^2 \langle \delta^2 \rangle_{\ell mn}^m] \\ & \cos 2\pi h_1 \ell \cos 2\pi h_2 m \\ & + 8\pi^2 N \sum_{\ell} \sum_m \sum_n h_1 h_2 \langle \delta^2 \rangle_{\ell mn}^{\ell m} \sin 2\pi h_1 \ell \sin 2\pi h_2 m \end{aligned} \quad (2)$$

The detailed derivation is presented by Epperson.<sup>(42)</sup> Relative to an arbitrarily chosen origin, the average interatomic vector is given by

$$\langle \mathbf{R}_{\ell mn} \rangle = \ell \frac{\hat{a}_1}{2} + m \frac{\hat{a}_2}{2} + n \frac{\hat{a}_3}{2} \quad (3)$$

where  $\ell$ ,  $m$  and  $n$  are integers and  $\hat{a}_1$ ,  $\hat{a}_2$  and  $\hat{a}_3$  are the translation vectors of a cubic unit cell. The continuous variables in reciprocal space,  $h_1$ ,  $h_2$  and  $h_3$ , are related to the diffraction vector by the relationship

$$\frac{\hat{\mathbf{S}} - \hat{\mathbf{S}}_0}{\lambda} = h_1 \hat{b}_1 + h_2 \hat{b}_2 + h_3 \hat{b}_3 \quad (4)$$

where  $\hat{b}_1$ ,  $\hat{b}_2$  and  $\hat{b}_3$  are vectors reciprocal to  $\frac{\hat{a}_1}{2}$ ,  $\frac{\hat{a}_2}{2}$  and  $\frac{\hat{a}_3}{2}$ . The Warren order parameter  $\alpha_{\ell mn}$  is

$$\alpha_{\ell mn} = 1 - \frac{P_{\ell mn}^{\text{BA}}}{X_B} \quad (5)$$

where  $P_{\ell mn}^{\text{BA}}$  is the conditional probability of finding a B atom as an  $(\ell mn)$  neighbor

of an A atom. Since the x-ray beam samples many atom pairs, the measured order parameters are averaged over many atom pairs contained in many coordination shells. Thus, every A atom does not have the same number of B atoms in the first shell or any other shell unless the alloy shows perfect long-range order. The alloy is composed of regions showing local order, but they do not have exactly the same local arrangement differing slightly from region to region in the sample. The size of the region over which local order exists is reflected by the convergence of the order parameters. The atomic displacement parameters or  $\gamma$ 's are defined as follows

$$\gamma_{\ell mn}^{\ell} = \frac{2\pi}{(f_A - f_B)} \left\{ \left( \frac{X_A}{X_B} + \alpha_{\ell mn} \right) f_A L_{\ell mn}^{AA} - \left( \frac{X_B}{X_A} + \alpha_{\ell mn} \right) f_B L_{\ell mn}^{BB} \right\} \quad (6)$$

where the superscript  $\ell$  on  $\gamma$  refers to one of the three cube axes, the strain parameter  $L_{\ell mn}^{AA}$  is the fraction of half the cube axis dimension that an A atom has been separated in excess of the average interatomic vector identified by  $\ell mn$  (negative if less separation);  $f_A$  and  $f_B$  are the atomic scattering factors of atoms A and B of atomic fraction  $X_A$  and  $X_B$ , respectively.

The atomic displacement  $\delta_{\ell mn}^{AA}$  is given as

$$\delta_{\ell mn}^{AA} = L_{\ell mn}^{AA} \left( \frac{\hat{a}_1}{2} + \frac{\hat{a}_2}{2} + \frac{\hat{a}_3}{2} \right) \quad (7)$$

where  $\hat{a}_1 = \hat{a}_2 = \hat{a}_3$  are the three cube axes. A relationship exists among the displacements for A-A, A-B and B-B pairs for each coordination shell which results from the necessity to conserve volume<sup>(34)</sup> and is given as

$$2X_A p_{\ell mn}^{BA} \delta_{\ell mn}^{BA} = - \left[ X_A (1 - p_{\ell mn}^{BA}) \delta_{\ell mn}^{AA} + X_B \left( 1 - \frac{X_A}{X_B} p_{\ell mn}^{BA} \right) \delta_{\ell mn}^{BB} \right] \quad (8)$$

As Equation 6 contains two unknown parameters, it is not possible to determine either one unambiguously from one set of data taken at one x-ray wavelength. However, plausible assumptions can be made about the relative magnitude of these two terms after determining the short-range order.

The mean-square displacement parameters  $\langle \delta \rangle_{\ell mn}$  and  $\langle \delta \rangle_{\ell mn}^{\ell}$ , describe the mean-square thermal and static displacements. The superscript indicates the coordinate direction in the real space lattice and the subscripts specify the coordinates of the atom at site p relative to site q. Equation 2 represents a generalization by Borie and Sparks<sup>(41)</sup> of the treatment of temperature diffuse scattering, second order size effect by Huang,<sup>(43)</sup> and short-range order due to Cowley<sup>(1)</sup> which had been modified by Warren, Averbach and Roberts,<sup>(2)</sup> to include the first order size effect. The treatment by Borie and Sparks<sup>(41)</sup> takes advantage of the fact that atomic order and atomic displacement modulations exhibit different symmetry in reciprocal space to separate the diffuse intensity associated with the  $\alpha$ 's,  $\gamma$ 's and  $\delta$ 's.

As our x-ray data were only measured in one plane of reciprocal space, two dimensional parameters  $A_{\ell m}$  are defined in terms of the three dimensional parameters,

$$A_{\ell m} = \sum_n \alpha_{\ell mn} \quad (9)$$

The displacement parameter gives the average of the distances between all A-B, A-A or B-B atom pairs for a constant interatomic vector. This is referred to as the size effect term and was first treated by Warren, Averbach and Roberts.<sup>(2)</sup>

For two dimensional data, one obtains the size-effect terms given as

$$\Gamma_{\ell m}^{\ell} = \sum_n \gamma_{\ell m n}^{\ell}; \Gamma_{\ell m}^m = \sum_n \gamma_{\ell m n}^m \quad (10)$$

## CHAPTER IV

### EXPERIMENTAL RESULTS AND DISCUSSIONS

#### A. Microscopic Fracture Processes

The microscopic fracture mechanism of the Ta-Nb and Mo-W alloys at ambient temperature are expected to be the same as their elements because the alloys do not solution harden. Scanning electron microscope fractographs of the elements and alloys were utilized to observe the effect of alloying on the microscopic fracture processes. Fractographs of ductile Ta and Nb single crystal fracture surfaces were characterized by slip pattern, small cup-and-cone fractures and tearing. Similar fracture topography has been reported for polycrystalline Nb by Wessel, France and Begley<sup>(44)</sup> and Ta single crystals by Raffo and Mitchell.<sup>(45)</sup> Figure 7A shows the same tearing and cup-and-cone fracture surface characteristics for the Ta-30 at.% Nb alloy. An alloy of 30 at.% Nb in Ta did not produce cleavage fracture. The authors observed the cleavage fracture that had been reported for polycrystalline for Mo by Bechtold,<sup>(46)</sup> Lement and Kreder,<sup>(47)</sup> and Wilcox and Gilbert,<sup>(48)</sup> and Mo single crystals by Beardmore and Hull<sup>(49)</sup> at ambient temperature. The cleavage fracture for W of single crystals was reported by Beardmore and Hull<sup>(50)</sup> and a combination of cleavage plus intergranular fracture was reported for polycrystalline tungsten by Wronski and Fourdeux,<sup>(51)</sup> Gilbert<sup>(52)</sup> and Forster and Gilbert<sup>(53)</sup> was also observed by the authors. Figure 7B shows river pattern cleavage fracture in a Mo-30 at.% W alloy similar to the fracture surface found in Mo-30 wt.% W - 1 wt.% Ti by Ferriss, Rose and Wulff.<sup>(54)</sup> The cleavage fracture characteristics are similar for Mo, W and the Mo-W alloys. The fracture surface



characteristics of Ta-Nb and Mo-W alloys formed from like sized atoms are the same as for the elements.

The Ta-Mo, Ta-W, Nb-Mo and Nb-W alloys are formed from atoms having about 5% difference in atomic size. Alloying Ta and W results in cleavage fracture at 300 K for alloys with greater than 30 at. % W as reported by Ferriss, Rose and Wulff.<sup>(54)</sup> Cleavage fracture was observed in Nb-50 at. % Mo single crystals and probably would be expected in alloys with as little as 30 at. % Mo because of the sharp reduction in ductility as reported by Milne and Smallman.<sup>(11)</sup> A combination of intergranular fracture and cleavage fracture was observed in polycrystalline Nb-14 at. % W (Fig. 7C) and Nb-33 at. % W in addition to W. Cleavage fracture at 300 K is therefore expected in Nb-W alloys containing more than 14 at. % W. Cleavage fracture was observed at ambient temperature for compositions ranging from Ta-9 at. % Mo (Fig. 7D) to pure Mo. Alloying 10 at. % to 30 at. % Mo or W with either Ta or Nb produces a transition in fracture surface characteristics from tearing, wavy flow and cup-and-cone topography to cleavage and intergranular fracture at ambient temperature. The strain fields around the solute atoms with their inherent 5% atomic size difference and the short range ordered atomic arrangement inhibit the dislocation movement or plastic flow near the crack tip thus causing the cleavage fracture.

In conclusion, the random solid solution Ta-Nb alloys exhibit the same ambient ductile fracture characteristics that were found in the Ta and Nb elements. The Mo-30 at. % W solid solution formed from like sized atoms showed the same ambient cleavage fracture that was previously observed for the Mo and W elements and the Mo-W alloys. Dissolving more than 10 to 30 at. % Mo or W in

either ductile Nb or ductile Ta at 300 K was found to produce a transition from ductile fracture to cleavage fracture.

#### B. Lattice Parameter of Ta-Mo Alloys

Figure 8 shows a negative deviation in lattice parameter from Vegard's Law for measurements by Geach and Summers-Smith<sup>(5)</sup> and the present authors. The measurements of Van Torne and Thomas<sup>(55)</sup> shown in Figure 8 have a positive deviation from Vegard's Law. Van Torne and Thomas<sup>(55)</sup> grew their single crystals using an electron beam zone melting at a zone speed of 25.4 mm/min. They assumed the crystal compositions to be the same as the starting composition or no preferential molybdenum evaporation during zone melting. Conversely, I observed evaporation weight losses of the more volatile molybdenum in all cases. Geach and Summers-Smith<sup>(5)</sup> also measured the chemical composition of their x-ray diffraction samples. Thus the apparent positive deviation from Vegard's Law found by Van Torne and Thomas<sup>(55)</sup> was caused by neglecting to measure the molybdenum weight loss in their crystals. The lattice parameter versus alloy composition should show a negative deviation from Vegard's Law for all Ta-Mo alloys.

#### C. Diffracted Intensity from Ta-Mo Alloys Along the $h_1, 0, 0$ Axis

The diffracted x-ray intensity measured along the  $h_1, 0, 0$  line in reciprocal space for Mo-21 at. % Ta, Mo-37 at. % Ta and Mo-91 at. % Ta is shown in Figure 9. The background x-ray intensity measured along the  $h_1, 0, 0$  line on Mo and Ta was about 40 counts per 120 sec and 60 counts per 120 sec respectively. Short range order peaks are clearly shown near the (100) and (300) reciprocal lattice positions for Mo-21 at. % Ta and Mo-37 at. % Ta. The peaks

heights for the Mo-37 at .% Ta alloy are much higher than for Mo-21 at .% Ta because of an increase in the degree of order and in the higher alloy content. The shift of the (100) and (300) order peaks to higher  $h_1$  values is a result of size effect. According to Warren and Averbach,<sup>(56)</sup> a low background between the (200) and (300) positions followed by a high background between the (300) and the (400) results also from size effect. Low background between the (200) and (300) followed by a high background between (300) and (400) is evident for each crystal. Figure 9 shows diffuse intensity at the leading edge of the (200) and (400) Bragg peaks for Mo-91 at .% Ta. This diffuse intensity can be explained by a combination of short range order and atomic displacement modulation. The preliminary diffuse x-ray measurements along the  $h_1 0, 0$  line shows that the Ta-Mo alloys possess short range order and size effect.

D. Diffuse X-Ray Scattering from the  $h_1 h_2 0$  Plane of Reciprocal Space from Ta, Mo and Ta-Nb Alloy

The total diffracted intensity from the  $h_1 h_2 0$  plane in reciprocal space was measured from Mo and Ta and is shown in Figures 10 and 11, respectively. The very large intensity peaks at the 200, 400, 110 and 220 positions are Bragg or fundamental peaks. A minimum uniform intensity of 50 counts per 30 sec for Mo and 75 counts per 30 sec for Ta was found near the 300, 210 and 320 order points. The same incident beam power was used for Mo, Ta and Nb-22 at .% Ta. It produced a diffracted intensity from polystyrene at  $2\theta = 100^\circ$ ,  $\chi = 0^\circ$ ,  $\omega = 0^\circ$  of 1400 counts per 30 sec. The intensity at these superstructure points is primarily incoherent scattering and temperature diffuse scattering. The intensity is larger for Ta because the coherent and incoherent scattering factors are both larger while the Debye temperature is lower.

The Ta crystal gave an intensity band between the 220, 310 and 400 Bragg peaks whereas Mo does not. The temperature diffuse scattering is larger for Ta because of the low Debye temperature and soft elastic constants as pointed out by Walker and Keating.<sup>(57)</sup> Mo, however, has a high Debye temperature and therefore lower  $I_{TDS}$  which the absence of interconnecting intensity band.

Surface oxides or reaction products that may be reacted with Ta or Mo would produce extra peaks. The total absence of extra peaks indicates the surface oxides are too thin to produce any effect on the diffraction pattern.

The Nb-22 at .% Ta alloy gave an x-ray diffraction pattern very similar to that of Ta (Fig. 12). The intensity connecting the 220, 310, and 400 Bragg peaks resulted from the large temperature diffuse scattering associated with the low Nb Debye temperature. A very large, uniform increase to 100-125 count per 30 sec covering the 300, 210 and 320 order peaks was found. The scattering factor of Nb (41 at  $2\theta = 0^\circ$ ) is similar to Mo (42 at  $2\theta = 0^\circ$ ) so one would expect a diffracted intensity of about 50 to 60 counts per 30 sec. An increased diffracted intensity from Nb-22 at .% Ta of 100-125 counts per 30 sec above Mo at 50 counts per 30 sec is 50-75 counts per sec was spread uniformly over the  $h_1 h_2 0$  plane. This Laue monotonic diffuse intensity is caused by the large difference in scattering factors between Nb (41 at  $2\theta = 0^\circ$ ) and Ta (73 at  $2\theta = 0^\circ$ ), and it is expressed mostly by the first two sums of Equation 2. It is possible to have atomic displacements in the alloy and no diffuse intensity if in Equation 6 the positive and negative terms cancel. The uniformly distributed Laue monotonic intensity shows the order and atomic displacement on the average of all atom pairs of the same coordination shell to be near zero. Thus, the alloy is nearly a random solid solution.

### E. Scattering from the $h_1 h_2 0$ Plane of Reciprocal Space from Ta-Mo Alloys

The total diffracted intensity for Mo-91 at .% Ta was measured using the same incident intensity and is shown in Figure 13. Short range order peaks corresponding to the 300 position and the 210 position are shifted away from the 300 and 210 order positions in the (110) direction due to the atomic displacement effects. The Bragg peaks are round rather than elliptical when compared to the Ta data. This could result from the Huang diffuse intensity which arises from the quadratic term in the atomic displacements<sup>(43)</sup> as it is known to increase in intensity near the Bragg peaks in the radial direction from the origin.

The diffuse x-ray scattering from the  $h_1 h_2 0$  plane in reciprocal space from Mo-21 and Mo-37 at .% Ta was measured. A correction for Compton incoherent scattering was computed using the incoherent scattering factors calculated by Cromer<sup>(58)</sup> and Cromer and Mann<sup>(59)</sup> and subtracted. An estimate of the parasitic air scattering was subtracted. The intensity around the Bragg peak including the Huang scattering and part of the TDS scattering was separated from the total intensity by smooth extrapolation of the diffuse short range peak through the Bragg positions. The partially corrected data for Mo-37 at .% Ta is similar to the Mo-21 at .% Ta alloy and are plotted in Figures 14 and 15, respectively. For Mo-21 at .% Ta and Mo-37 at .% Ta, the atomic displacement effect caused the 210 short range order peak to shift away from the origin in the (110) direction by about 0.1 times the lattice parameter. This shift in the Mo-91 at .% Ta alloy is 0.2 times the lattice parameter. Epperson and Spruiell<sup>(60)</sup> also found a shift in the short range order peak induced by the atomic displacement effect because of atomic displacements for Fe rich Al alloys.

The data from the Mo-21 and Mo-37 at .% Ta alloys was corrected for absorption by measuring the total intensity near the short range order peaks before and after the crystal was rotated  $180^\circ$  about an axis normal to the crystal face and taking the mean value. The intensity measurements were converted to absolute units (electron units per atom)  $I_{eu}/N$  using the technique of Warren and Averbach.<sup>(56)</sup> The diffuse intensity was separated into the short range order component and the atomic displacement component for both the linear and quadratic terms using the computer programs of Epperson.<sup>(60)</sup> The short range order coefficients and atomic displacement coefficients were calculated, and reported in Tables III, IV and V.

The  $A_{00}$  coefficients for both Mo-21 and Mo-37 at .% Ta are very low. This resulted from using diffuse intensity values that were too low. The estimates of parasitic scattering and absorption were too high; therefore, the diffuse intensity remaining after these terms were subtracted was too low. This leads to somewhat less accurate  $A_{\ell m}$  values. The  $A_{\ell m}$  values for Mo-37 at .% Ta were calculated using a linear separation<sup>(42)</sup> from the data bounded by  $h_1, h_2$  coordinates (0.5, 0; 0.5, 0.5; 1, 1; 1, 0) in Figure 14. The  $A_{\ell m}$  short range order coefficients calculated from the linear separation agreed well with the  $A_{\ell m}$  values from the quadratic separation which utilizes data bounded by the coordinate (0.5, 0; 0.5, 0.5; 1, 1; 1.5, 1; 1.5, 0). Agreement between the  $A_{\ell m}$  short range order coefficients determined from the linear and quadratic separation indicates there are no significant errors introduced to the coefficients  $A_{11}$  through  $A_{44}$  because of the quadratic terms.

Comparison of the signs of the experimental  $A_{\ell m}$  values for Mo-21 and Mo-37 at .% Ta with the signs on both the long range ordered (LRO) Mo-Ta and  $\text{Mo}_3\text{Ta}$  structures shows good agreement from  $A_{00}$  through the  $A_{40}$  except for  $A_{33} = 0.001$  for Mo-37 at .% Ta which is near zero. This shows that both Mo-21 and Mo-37 at .% Ta alloys have a similar short range order distribution of atoms. These short range ordered alloys tend to form one or a combination of the (B-2) or ( $\text{DO}_3$ ) long range ordered structures found in body centered cubic systems. However, the two dimensional short range order coefficients for both the Mo-Ta (B2) structure and  $\text{Mo}_3\text{Ta}$  ( $\text{DO}_3$ ) structure have the same sign variation. Thus the measured two dimensional  $A_{\ell m}$ 's for the alloys cannot be used to predict whether the alloys tend toward a (B2) or a ( $\text{DO}_3$ ) structure.

The atomic displacement coefficients are reported in Table IV and Table V. The atomic displacement coefficients for both Mo-21 and Mo-37 at .% Ta have the same sign from  $\Gamma_{11}^1$  through  $\Gamma_{44}^4$  except for  $\Gamma_{44}^4$  for the Mo-37 at .% Ta alloy. With that exception, all the atomic displacement coefficients are positive for  $M = 1$  and  $M = 3$  and negative for  $M = 2$  and  $M = 4$ . The similarity of the sign variation of the atomic displacement coefficients and rate of convergence indicates the atomic displacement effect is similar for both alloys.

#### F. Short Range Order in the Mo-37 at .% Ta and Mo-21 at .% Ta

To determine local atomic arrangements with alloying compositions, we fitted as best we could an atom model of Mo-37 at .% Ta alloy and Mo-21 at .% Ta alloy to the  $A_{\ell m}$ 's. The ordered Mo-37 at .% Ta alloy crystal is described by a model containing 99 atoms in the crystal. The (100) planes shown in Figure

16 are stacked on top of each other. Plane II is sandwiched between planes I and III to form the model. Molybdenum atoms are represented by closed circles and tantalum by open circles. Each box is occupied by 54% Ta. The boxes enable the model to conserve composition. The unoccupied sites of the model are atoms having the average alloy composition of 37% Ta. The model of the Mo-21 at .% Ta alloy contains 89 atoms and is formed by sandwiching plane B between planes A and C in Figure 17. The models are created by trial and error. The three dimensional short range order coefficients ( $\alpha_{\ell mn}$ ) are calculated from the model and summed according to Equation 8 to obtain the two dimensional  $A_{\ell m}$  values as shown in Table VI. In order to get reasonable agreement between the measured and calculated  $A_{11}$  values, very few Ta-Ta first nearest neighbors could be permitted. In order to calculate positive values of  $A_{20}$  and  $A_{22}$ , a preference for Ta-Ta (200), (220) and (222) neighbors was necessary in each model. Cubic metals have a high degree of symmetry which is not exhibited by the models having the dimensions of three atomic layers high by six or seven atomic layers wide. These models may be located at random on any of the three (100) planes to increase the symmetry so as to encompass about 150 atoms.

The models for Mo-21 and 37 at .% Ta alloys were calculated independently. The probability of finding a Mo atom in the (111) position with respect to a Ta atom would range from 79% to 100% if the first nearest neighbors of the Mo-21 at .% Ta alloy varied from random to fully ordered, and from 63% to 100% if the Mo-37 at .% Ta alloy varied from random to fully ordered. The probability of finding a Mo atom in the (111) position with respect to a Ta atom was calculated

from the models and found to be 85% for Mo-21 at .% Ta and 72% for the Mo-37 at .% Ta. For both alloys this is about 25% of the range for first nearest neighbor between a random solid solution and the perfectly ordered solution. The measured short range order parameters converge to near zero for  $A_{44}$  for both alloys. The common convergence of the short range order parameters as well as the common sign variation shows that the short range ordered structure is similar in both alloys. The convergence of the short range order coefficients to zero gives a measure of the size of the region about an atom in which the short range order persists. Similarly, the extent to which a cooperative (coordinated) strain field exists about an atom is measured by the convergence to zero of the atomic displacement parameters. This occurs near the 442 shell for both the order and atomic displacement and encompasses about 150 atoms. In fact, the model of the short range order in the Ta-Mo alloys is very much like that for Fe-Al alloys,<sup>(60)</sup> both having a tendency to avoid the like nearest neighbors.

#### G. Atomic Displacement Effect for Mo-Ta Alloys

The atomic displacement coefficients are reported in Tables IV and V. They are similar in sign but not in magnitude. With the exception of  $\Gamma_{44}^4$ , the coefficients are positive for  $M = 1$  and 3 and negative for  $M = 2$  and 4. Note that for the first coefficients the displacement coefficients have a sign opposite to that of the short range order coefficients. In general, the lower order coefficients are largest and the predominant contribution to the two dimensional coefficients are most likely the lowest-order three dimensional coefficients. Assuming this to be the case, these shells for which the short range order coefficients are negative have a preference to be unlike neighbors to the origin atom compared to that of a random alloy.

The positive short range order coefficients indicate the origin atom prefers like neighbors for that shell. To understand the sign and magnitude of the displacement coefficients, we need to put known parameters in Equation 6 and determine the relative contributions of the two terms. Let the A atom represent Ta and B atom represent Mo. The two terms (Expression 11) in Equation 6 are

$$\left( \frac{X_{Ta}}{X_{Mo}} + \alpha_{\ell mn} \right) f^{Ta} L_{\ell mn}^{TaTa} - \left( \frac{X_{Mo}}{X_{Ta}} + \alpha_{\ell mn} \right) f^{Mo} L_{\ell mn}^{MoMo} \quad (11)$$

which for the  $\ell mn = 111$  of the Mo-37 at .% Ta alloy gives approximately  $(0.59 - 0.36) f^{Ta} L_{111}^{TaTa} - (1.7 - 0.36) f^{Mo} L_{111}^{MoMo}$ . The average values of  $f^{Ta}$  and  $f^{Mo}$  for the range of  $2\theta$  at which the data were taken are 30 and 50 respectively. With these values, our two terms become  $11.5 L_{111}^{TaTa} - 40.2 L_{111}^{MoMo}$ . Since our measured  $\Gamma_{11}^1$  was positive (+0.80) and Mo is the smaller atom, we expect  $L_{111}^{MoMo}$  to be negative. For the alloy containing 21 at .% Ta, the two terms become  $3.8 L_{111}^{TaTa} - 107 L_{111}^{MoMo}$  which makes the strain associated with the Mo-Mo pairs the most dominant feature of the size effect intensity. In going from 0.37 at. fraction of Ta to 0.21, the observed displacement coefficient went from 0.080 to 0.240 ratio. For the Mo-91 at .% Ta alloy, the dominance of one of the two terms in the displacement coefficient becomes very large as the two terms are  $500 L_{111}^{TaTa} - 0$  if we set  $\alpha_{111} = -0.1$  through its value has little effect on the result. Since  $\Gamma_{11}^1$  must be positive to shift the SRO diffuse peaks away from the origin in reciprocal space, the  $L_{111}^{TaTa}$  must to be positive because the Ta-Ta first nearest neighbors are farther apart than the average (111) interatomic vector. The large multiplying factor of 500 accounts for the large shift observed in the x-ray measurements for the Mo-91 at .% Ta alloy,

(Fig. 13). Similar arguments can be made for the  $\Gamma_{02}^2$  terms which are negative and represent predominantly second nearest neighbors. Thus Mo-Mo neighbors distances are larger than the average (200) interatomic vector and the Mo atoms also prefer like neighbors in their second shells. The pattern of a preference for the like neighbors signifying larger than average interatomic distances and a preference for unlike neighbors having closer than average distances persists through the fourth neighbors. The Ta atoms act as dilatation centers to its nearest neighbors and Mo is a contraction center for Mo-Mo neighbors pairs.

When the probability of finding an A-B first nearest neighbor (111) for a BCC alloy is about 100% as is indicated by the short range order parameter, the first atomic displacement ( $\gamma_{111}^1$ ) can be approximated with a hard sphere model as found by Epperson and Spruiell. (60) The probability of finding Mo (111) nearest neighbor adjacent to a Ta atom is 72% for Mo-37 at .% Ta and 85% for Mo-21 at .% Ta. These values are less than 100% but show a very strong preference for Mo-Ta nearest neighbors. These atomic displacements were compared with a hard sphere model to aid in the explanation of the atomic displacement modulations associated with first nearest neighbors. Knowing the lattice constant of the alloys (Fig. 8) and the lattice constant of Mo and Ta, one may calculate the expected difference for the interatomic vector of the Mo-Mo pairs, Ta-Ta pairs and Ta-Mo pairs. These values are listed in Table VII.

For the Mo-21 at .% Ta alloy, the atomic displacement terms calculated from the hard sphere model gave:  $\delta_{111}^{MoMo} = -0.0040 \left( \frac{a_1}{2} + \frac{a_2}{2} + \frac{a_3}{2} \right)$  and  $\delta_{111}^{MoTa} = 0.0101 \left( \frac{a_1}{2} + \frac{a_2}{2} + \frac{a_3}{2} \right)$ . For the Mo-37 at .% Ta alloy the atomic displacement terms calculated from the hard sphere model gave:  $\delta_{111}^{MoMo} = -0.0073 \left( \frac{a_1}{2} + \frac{a_2}{2} + \frac{a_3}{2} \right)$

and  $\delta_{111}^{MoTa} = 0.0054 \left( \frac{a_1}{2} + \frac{a_2}{2} + \frac{a_3}{2} \right)$ . For the Mo-91 at .% Ta alloy, the atomic displacement terms calculated from the hard sphere model gave:  $\delta_{111}^{TaTa} = 0.0037 \left( \frac{a_1}{2} + \frac{a_2}{2} + \frac{a_3}{2} \right)$  and  $\delta_{111}^{TaMo} = -0.010 \left( \frac{a_1}{2} + \frac{a_2}{2} + \frac{a_3}{2} \right)$ .

The rate of atomic displacement ( $\delta_{111}^{TaMo}$ ) change as a function of composition for Ta rich and Mo rich alloy is calculated using the hard sphere model. The atomic displacement from the average lattice site for the Ta solute ranges from 0.071Å to 0.047Å ( $L_{111}^{TaMo}$  from 0.0150 to 0.0099) for the Mo rich Ta alloys ranging in composition from Mo to Mo-25 at .% Ta. The atomic displacement from the average lattice site ( $\delta_{111}^{TaMo}$ ) for the Mo solute ranges from -0.063 to -0.020Å ( $L_{111}^{TaMo}$  from -0.0127 to -0.0041) for Ta to Ta-25 at .% Mo using the hard sphere model. The hard sphere model calculations show twice the rate of atomic displacement change or elastic strain term change for Mo dissolved in Ta as for Ta dissolved in Mo. This correlates well with the fact that solution hardening rate for Ta rich Mo alloys (1.7 kg/mm<sup>2</sup> per atomic percent) have a solution hardening rate that is proportionately higher than the Mo rich Ta alloys (1.2 kg/mm<sup>2</sup> per atomic percent) by about the same ratio. The larger rate of elastic strain term change in the Ta rich Mo alloys as calculated from the hard sphere model cause the atomic displacement to be greater in the Mo-91 at .% Ta alloy than either the Mo-21 at .% Ta alloy or the Mo-37 at .% Ta alloy.

If we assume that the coefficients are negligible beyond  $\Gamma_{24}^4$ , then we may write from Equation 10 that for Mo-21 at .% Ta alloy:

$$\Gamma_{11}^1 = 2\gamma_{111}^1 + 2\gamma_{311}^1 = 0.240$$

$$\Gamma_{31}^1 = 2\gamma_{311}^1 + \cancel{2\gamma_{331}^1} = 0.049$$

$$\gamma_{111}^1 = \frac{0.240 - 0.049}{2} = \frac{0.191}{2} \cong 0.095$$

Using Equation 6 for A as Ta and B as Mo:

$$\gamma_{111}^1 = \frac{2\pi}{50 - 30} \left[ \left( \frac{0.21}{0.79} - 0.19 \right) 50 L_{111}^{\text{TaTa}} - \left( \frac{0.79}{0.21} - 0.19 \right) 30 L_{111}^{\text{MoMo}} \right]$$

$$\gamma_{111}^1 = 0.314 (3.8 L_{111}^{\text{TaTa}} - 107 L_{111}^{\text{MoMo}}) = 0.095$$

$$L_{111}^{\text{MoMo}} = \epsilon_{111}^{\text{MoMo}} = \frac{-0.095}{33.6} = -0.0028$$

Using the same calculation for Mo-37 at .% Ta alloy:

$$\Gamma_{11}^1 = 2\gamma_{111}^1 + 2\gamma_{311}^1 = 0.080$$

$$\Gamma_{31}^1 = 2\gamma_{311}^1 + 2\gamma_{111}^1 = 0.004$$

$$\gamma_{111}^1 = \frac{0.080 - 0.004}{2} = 0.038$$

$$\gamma_{111}^1 = 0.038 = 0.314 \left[ \left( \frac{0.37}{0.63} - 0.36 \right) 50 L_{111}^{\text{TaTa}} - \left( \frac{0.63}{0.37} - 0.36 \right) 30 L_{111}^{\text{MoMo}} \right]$$

Assuming that  $L_{111}^{\text{TaTa}}$  has the same value for the Mo-37 at .% Ta alloy as for the Mo-21 at .% Ta:

$$\gamma = 0.038 = 0.314 (11.5 (-0.0028) - 40.2 L_{111}^{\text{MoMo}})$$

$$L_{111}^{\text{MoMo}} = -0.0038$$

The two dimensional atomic displacement terms were not recovered for the Mo-91 at .% Ta alloy so the  $L_{111}^{\text{TaTa}}$  cannot be calculated nor can  $L_{111}^{\text{MoTa}}$  or  $\delta_{111}^{\text{MoTa}}$  be calculated for all Mo-Ta alloy using Equation 8. From a similar calculation, the values for  $L_{\ell mn}^{\text{MoMo}}$ ,  $L_{\ell mn}^{\text{TaMo}}$ , and  $L_{\ell mn}^{\text{TaTa}}$  for the second, third and fourth nearest neighbors shells can be calculated. Two planes of diffuse x-ray data should be measured with different radiation and reduced from Ta rich Mo rich crystals to obtain the elastic strain value from the diffuse x-ray data. The two  $L_{111}^{\text{MoMo}}$  elastic strain values

in Table VII do agree in sign and somewhat in magnitude with the hard sphere model. When the strain parameters  $L_{\ell mn}^{\text{MoMo}}$ ,  $L_{\ell mn}^{\text{TaTa}}$  and  $L_{\ell mn}^{\text{TaMo}}$  are obtained from the Ta rich Mo alloys, the strain energy associated with the SRO region could be calculated. The interaction between dislocation strain field and chemical energy plus strain field of the SRO region would provide the basis for calculating the force necessary to move the dislocation through the SRO region or barrier.

#### H. Substitutional Solid Solution Hardening and Short Range Order Hardening

The Ta-Nb and Mo-W alloys have almost the same elemental atomic size, their lattice parameter is invariant with composition. They show no substitutional solid solution hardening. From the diffuse x-ray scattering measurements on Nb-22 at .% Ta, this alloy appears to be a random solid solution with the solute atoms located on the average lattice sites. All the Ta-Nb alloys are therefore expected to be random. Mo-W alloys are expected to exhibit a very small deviation from random solid solution due to their small elemental atomic size difference and limited high temperature solution hardening.<sup>(23)</sup> An absence of substitutional solid solution and short range order hardening is observed when solutions were formed from equal sized atoms with large differences in their shear modulus values.

The Ta-Mo, Ta-W, Nb-Mo and Nb-W binary alloys with about 5% difference in their atomic size show a lattice parameter variation with composition, a negative deviation from Vegard's Law and linear hardening extended to high solute concentrations at room temperature. The linear hardening rate of the low modulus Ta or Nb alloys were found to be 11 DPH values per at .% Mo or W or

1.7 kg/mm<sup>2</sup> per at .% Mo or W. Whereas the high modulus Mo alloys were found to harden at a lower rate of 8 DPH values per at .% Ta or Nb corresponding to about 1.2 kg/mm<sup>2</sup> per at .% Ta or Nb.

Flinn's<sup>(67)</sup> theory permits the calculation of short range order strengthening by ordered first nearest neighbors for FCC alloys. Using Flinn's<sup>(67)</sup> theory adjusted for BCC alloys, the SRO strengthening of only 0.5 kg/mm<sup>2</sup> for Mo-21 at .% Ta ( $\alpha_{111} = -0.069$  from the model) and of only 1.7 kg/mm<sup>2</sup> for Mo-37 at .% Ta ( $\alpha_{111} = -0.146$  from the model) was calculated. These strengthening values are very low when compared to the observed strengthening produced by the SRO and the solution hardening of about 25 kg/mm<sup>2</sup> for Mo-21 at .% Ta and about 44 kg/mm<sup>2</sup> for Mo-37 at .% Ta. If the SRO hardening calculated from Flinn's<sup>(67)</sup> theory is at all accurate, one can conclude that the predominant hardening mechanism in the Ta-Mo alloys is substitutional solid solution strengthening. Atomic size mismatch appears to be the dominant substitutional solid solution hardening parameter for Ta-Nb and Ta-Mo alloys as suggested by Rudman,<sup>(13)</sup> Harris,<sup>(15)</sup> and Chang.<sup>(14)</sup>

The current substitutional solid solution hardening theories are compared with the observed ambient temperature substitutional solid solution hardening rates of Ta-Nb alloys, Mo rich Ta alloys and Ta rich Mo alloys to calculate the hardening. The random solid solution hardening theories based on a dominant shear modulus effect by Fleisher,<sup>(16)</sup> Boser<sup>(18)</sup> and Labusch<sup>(61)</sup> describe hardening for dilute solutions at 0 K, while Suzuki<sup>(17)</sup> included concentrated solutions at high or plateau temperatures. The absence of solution hardening for Ta-Nb and W-Mo corresponding to an absence of atomic mismatch for Ta-Nb and W-Mo cannot be explained by the above theories. The room temperature

hardening is not explained by Mott and Nabarro<sup>(62)</sup> or Riddhaghi and Asimow<sup>(63,64)</sup> who calculate hardening at 0 K. Assuming the solution hardening for these BCC alloys at the plateau temperatures is high and about equal to the solution hardening at 0 K as shown for Ta-9 at % W by Arsenault,<sup>(24)</sup> the solution hardening calculated by Asimow<sup>(64)</sup> can be compared to the observed substitutional solid solution hardening. The substitutional solid solution hardening values calculated from Figures 1 and 2 and from the shear modulus values of Armstrong and Mordike<sup>(75)</sup> are found to be a factor of 4 to 8 times higher than predicted by Asimow<sup>(64)</sup> for a 1.5 type edge dislocation hardening. Asimow's<sup>(64)</sup> theory does agree with the FCC substitutional solid solution hardening and predicts the absence of hardening for Ta-Nb and Mo-W alloys. Foreman and Makin<sup>(65)</sup> predict no plateau hardening for dilute solutions. Friedel<sup>(66)</sup> predicts zero hardening with zero atomic size mismatch at high temperature, a near linear hardening rate or  $C^{4/3}$  but for dilute solutions. None of these theories explain the linear plateau substitutional solid solution hardening observed in these BCC alloys.

#### I. Suggestions for Future Research

With present data a solution hardening theory can be developed which would be based primarily on the atomic size mismatch effect as the barrier to dislocation motion in BCC solid solutions. The solid solutions could be assumed random. The solution hardening stress should be proportional to the atomic size mismatch and equal to zero when the atomic mismatch is equal to zero. The plateau stress could be explained by distributing the stress fields of the individual solute atoms along the full length of the dislocation thus preventing thermally activated dislocation movement.

The complexity of the atomic arrangements that are found in solid solutions (local order and atomic displacement) do not permit easy first principle calculation of the change in strength with concentration. Through x-ray diffuse scattering providing a better understanding of the atomic arrangements in solid solutions, the complexity of the atomic arrangements complicates the modeling and gives only an average configuration. If several regions in the alloy are sampled, we are not likely to find the same arrangement in any two of them.



That the solid solution has only short range order, by definition precludes the alloy from being compared to groups of atoms having a large superlattice which is not observed in Mo-Ta alloys. The SRO parameters ( $\alpha$ ) give us the average configuration of the local order. As  $\alpha \rightarrow 0$  for the more distant pairs, we have a measure of the size of the region of local order beyond which the probability of forming AA, AB and BB pairs becomes that of a random solid solution. The length of a dislocation line is measured in hundreds of Angstroms in many lattice distances which is much greater than the size of the local order region. However, a region of local order extends around each atom. The dislocation is subjected to local chemical order and correlated atomic displacements about each atom site along its length, yet from one part of the dislocation line to another only 10 lattice constants away, the dislocation has sampled enough atomic sites to experience the average structure.

With additional diffuse x-ray diffraction data, hardness or solution hardening strength measurements and elastic modulus values from the Ta rich Mo alloys and the Nb-V solid solutions, a solution hardening theory could be developed from the dislocation interaction with the observed atomic structure of the solution. The solution hardening of three types of alloys would be represented. The Nb-V alloys represent solution hardening for alloys formed from elements having the same modulus but different atomic size. The Ta-Nb solid solutions would exhibit solution hardening for alloys formed from elements having equal size atoms but unequal modulus values. The Ta-Mo solid solutions exhibit solid solution hardening when the alloy is formed from elements of unequal atomic size and unequal modulus. The theory could represent the alloys by a statistical distribution of atoms whose average distribution is equal to the measured SRO structure rather than a random atomic distribution. The average strain field in the theory caused by the atomic misfit in the alloys could be described by the average of a distribution atoms positioned off the atomic sites in such a

manner that their average strain terms equal the values measured by diffuse x-ray diffraction. Equating the total force on the dislocation imposed by external load on the crystal to the interaction force between the SRO region over a solute concentration range would permit the calculation of solid solution hardening. The chemical interaction energy and force on the dislocation in both the Ta rich and Mo rich alloys could be calculated using a short range order mechanism of the type of Flinn<sup>(67)</sup> modified to include all the observed SRO shells and the same dislocation interaction mechanism proposed for the solution hardening. The interaction energy and force created by the strain field of the dislocation and the strain field associated with the average atomic displacement in the SRO region could be calculated using the  $L_{\ell mn}^{TaTa}$ ,  $L_{\ell mn}^{MoMo}$  and  $L_{\ell mn}^{TaMo}$  strain terms using the first several shells and added to the interaction force caused by the short range order chemical energy to obtain the total dislocation-obstacle interaction force. Again a set of atomic displacement and associated strain terms from two Ta rich Mo alloys would be required. In addition, a direct measurement of each crystal shear moduli would provide a more accurate calculation of the dislocation interaction force (short range order atomic displacement region) and help remove the ambiguity of modulus effects on solution hardening. The distribution of the short range order and atomic displacement regions along the dislocation line and throughout the crystal which has the observed short range order and atomic displacement parameter values could be developed following Eshelby.<sup>(68)</sup> The increase in yield stress with Ta or Mo solute concentration could then be calculated from such a model by using the approach of Foreman and Makin.<sup>(65)</sup> The average size of the short range order region that interacts

with the strain field can be taken as about 10 lattice parameters or the diameter of the 442 shell. The strain parameters can be obtained from Table VII plus values to be calculated from the two Ta rich Mo alloys that need be measured.

The solid solution hardening calculations should equal the 1.7 kg/mm<sup>2</sup> per at .% Mo observed in Ta rich Mo alloys and 1.2 kg/mm<sup>2</sup> per at .% Ta for Mo rich Ta alloys. The hardening should be zero for the random Ta-Nb alloys when the atomic misfit is zero but the modulus difference is large. The substitutional solid solution hardening should also be present for the Nb-V BCC solutions with equal modulus and substantial atomic misfit as shown by Hobson.<sup>(69)</sup> If the correlation between the substitutional solid solution hardening theory and the observation were found to be good, the substitutional solid solution hardening theory would be expected to predict the hardening in the remaining Ta, Mo, W and Nb binary BCC solid solutions.

## CONCLUSIONS

The observed lattice parameters, substitution solid solution hardening and fracture properties of Nb, Ta, Mo and W binary solid solutions showed two types of behavior. Ta-Nb and Mo-W alloys formed from equal size atoms and different modulus have lattice parameters that obey Vegard's Law, show an absence of substitutional solid solution hardening and exhibit an absence of fracture embrittlement at high solute concentrations. The Ta-Mo, Ta-W, Nb-Mo and Nb-W binary solid solutions having a 5% difference in their elemental atomic size show a negative deviation in Vegard's Law, linear solid solution hardening to high solute concentrations at room temperature and fracture embrittlement at high alloy concentrations. These observations agree with the data reported in the literature. The diffuse x-ray measurement of the Nb-22 at .% Ta alloy from the alloy type having equal size atoms showed the alloy to be a random solid solution. Diffuse x-ray measurement of the Ta-Mo alloys of the alloy type with 5% difference in atomic size showed short range order and atomic displacement to the (442) shell. Models of the Mo-21 at % Ta and the Mo-37 at % Ta alloys were established to describe the similar distribution of the short range ordered atoms. Because the short range order accounts for less than 5% of the alloy strengthening and the x-ray data shows very large atomic size effects, the large Ta-Mo strengthening is attributed to the substitutional solid solution hardening controlled by atomic size mismatch extending to the (442) shell. The solution hardening rate of ~~Ta Mo~~ dissolved in ~~Mo~~<sup>Ta</sup> was shown to be higher than ~~Mo~~<sup>Ta</sup> dissolved in ~~Ta~~<sup>Mo WHICH IS IN</sup> agreement with the hard sphere model but not confirmed by x-ray measurement.

Table I

## Zone Melting and Crystal Growth Conditions

Melt Number	Crystal Sample Number	Charge Description	Zone Melting Procedure and Minimum Pressure	Charge Composition (Atomic %)	Crystal Composition (Atomic %)	Relative Evaporation Loss (Atomic %)	Crystal Size
Mo-Ta Alloys							
Melt I	B-IV	6.3 mm Diam. Mo Rod	3 Passes $7 \times 10^{-9}$ torr	100% Mo	100% Mo	—	3 Crystals about 21 mm Long x 6 mm Diam.
Melt II	B-VII-2 B-VII-4 B-VII-6 B-VII-8 B-VII-5	6.3 mm Diam. Mo Rods with 2-1.6 mm Diam. Ta Wires	4 Passes $5 \times 10^{-10}$ torr 2.7 mm/min	Mo-15% Ta	Mo-20.1% Ta Mo-215% Ta Mo-20.5% Ta Mo-17.6% Ta Mo-20.5% Ta	5% Mo	2 Single Crystals plus Large Polycrystals
Melt III	B-VI-1 B-VI-3 B-VI-4 B-VI-5	6.3 mm Diam. Mo Rods with 3-1.6 mm Diam. Ta Wires	4 Passes $10^{-9}$ torr 3.5 mm/min	Mo-17% Ta	Mo-27.7% Ta Mo-39.5% Ta Mo-40.5% Ta Mo-36.3% Ta	20% Mo	2-25 mm Long Crystals plus Large Polycrystals
Melt IV	B-III	4.8 mm Mo-Ta Alloy Rod (B-II) Plus 15-0.8 mm Diam. Mo Wires	3 Passes $2 \times 10^{-8}$ torr 3 mm/min	Ta-31% Mo	Ta-9.3% Mo	22% Mo	1-4.3 mm Diam. Crystal x 50 mm Long

Table I (Continued)

Melt Number	Crystal Sample Number	Charge Description	Zone Melting Procedure and Minimum Pressure	Charge Composition (Atomic %)	Crystal Composition (Atomic %)	Relative Evaporation Loss (Atomic %)	Crystal Size
Melt V	B-I	6.3 mm Ta Rod Plus 0.8 mm Diam. Mo Wires	3 Passes $10^{-8}$ torr 3 mm/min	Ta-11% Mo	Ta-3.9% Mo	7% Mo	5 Single Crystals 150 mm Long
Melt VI	B-II	B-1	2 Passes $10^{-8}$ torr 3 mm/min	Ta-39% Mo	Ta-0.8% Mo	3% Mo	Single Crystal 150 mm Long
Melt VII	B-V	9.5 mm Diam. Ta Rod	2 Passes $10^{-8}$ torr 3 mm/min	100% Ta	100% Ta	—	Single Crystal
Mo-W Alloys							
Melt VIII	B-XV-7 B-XV-19	6.3 mm Diam. Mo Rod Plus 3-1.6 mm Diam. W Wire	4 Passes $10^{-7}$ torr 12 mm/min 1.2 mm/min	Mo-19% W Mo-30% W	Mo-20% W	1% Mo 11% Mo	Polycrystal 0.3 mm ave. Grain Diam. Polycrystal 0.5 mm ave. Grain Diam.

Table I (Continued)

Melt Number	Crystal Sample Number	Charge Description	Zone Melting Procedure and Minimum Pressure	Charge Composition (Atomic %)	Crystal Composition (Atomic %)	Relative Evaporation Loss (Atomic %)	Crystal Size
Nb-W Alloys							
Melt IX	B-XII	6-3 mm Diam. Nb Rod Plus 2 1.6 mm Diam. W Wires	5 Passes $5 \times 10^{-9}$ torr 2.5 mm/min	Nb-14% W	Nb-14% W	None	Polycrystal 0.5 mm ave. Grain Diam.
M-X	B-X-2	6.3 mm Diam. Nb Rod Plus	3 Passes $5 \times 10^{-9}$ torr	Nb-30% W	Nb-29% W	None	Polycrystal 0.2 mm ave. Grain Diam.
	B-X-5	4-1.6 mm			Nb-32.7% W		
	B-X-6	Diam. W			Nb-29.8% W		
	B-X-8	Wires			Nb-29.8% W		
Nb-Ta Alloys							
M-XI	B-XVI	6.3 mm Nb Plus 3 Ta Wires	5 Passes $2 \times 10^{-8}$ torr 1.3 mm/min	Nb-20% Ta	Nb-23% Ta	3% Nb	Polycrystal 1.5 mm ave. Grain Diam. Plus 1-Crystal
M-XII	B-XI-2	6.3 mm Nb Rod Plus	3 Passes $9 \times 10^{-8}$ torr	Nb-29% Ta	Nb-33.4% Ta	Unknown Residual	Polycrystal 0.5 mm ave. Grain Diam.
	B-XI-4	4 Ta Wires	1.3 mm/min		Nb-29.8% Ta	Ta Wires	
	B-XI-6	(1.6 mm Diam.)			Nb-30.1% Ta		
	B-XI-8				Nb-29.2% Ta		

42

Table II  
Diffuse X-Ray Measurement Conditions

Crystal	Orientation	Scan. Pat.	Data Points	Slit	X-Ray Power	Count Rate
					KVP MA	Polystyrene 20 = 100°
Mo (100)	B = 9°		40	0.02°	40 20	
Ta (100)	B = 9°		40	0.02°	40 20	
Ta-91 a/o Mo (100)	B = 0.9°		40	0.02°	40 20	
Mo-21 a/o Ta (100)	B = 0.9°		40	0.02°	40 20	
Mo-37 a/o Ta (100)	B = 0.9°		54	0.02°	40 20	
Mo (100)			800	0.2°	30 15	1191 counts 30 sec
Ta (100)			800	0.2°	30 15	1400 counts 30 sec
Ta-9 a/o Mo (100)	B = 1.6°		1800	0.2°	30 15	1385 counts 30 sec
Mo-37 a/o Ta (100)	B = 0.9°		1350	0.02°	30 15	468 counts 60 sec
Mo-21 a/o Ta			1000	0.02°	40 20	761 counts 60 sec
Nb-22 Ta			570	0.2°	40 20	1412 counts 30 sec

43

Table III

## Two Dimensional Short-Range Order

Parameters  $A_{\ell m}$  For the Mo-21 and Mo-37 at .% Ta Alloys

$A_{\ell m}$	Mo-37 at .% Ta	Mo-21 at .% Ta	Signs from Perfect MoTa LRO (B2) and Mo <sub>3</sub> Ta (DO <sub>3</sub> )	Fe - 18.3 at .% AL <sup>30</sup>
	Experimental	Experimental	Calculated	Experimental
$A_{00}$	0.638	0.284	+	1.145
$A_{11}$	-0.356	-0.190	-	0.412
$A_{20}$	0.208	0.138	+	0.273
$A_{22}$	0.048	0.051	+	0.138
$A_{31}$	-0.041	-0.056	-	-0.115
$A_{33}$	0.001	-0.007	-	-0.089
$A_{40}$	0.026	0.053	+	0.069
$A_{42}$	-0.003	0.018	+	0.052
$A_{44}$	-0.009	0.004	+	0.030

Table IV

## Atomic Displacement Coefficients

 $\Gamma_{\ell m}^m$  For Mo-37 at .% Ta

$\ell$	$m = 1$	$m = 2$	$m = 3$	$m = 4$
0	0.000	-0.134	0.000	-0.070
1	0.080	0.000	0.081	0.000
2	0.000	-0.045	0.000	-0.032
3	0.004	0.000	0.017	0.000
4	0.000	-0.005	0.000	0.012

Table V

## Atomic Displacement Coefficients

 $\Gamma_{\ell m}^m$  For Mo-21 at .% Ta

$\ell$	m = 1	m = 2	m = 3	m = 4
0	0.000	-0.210	0.000	-0.056
1	0.240	0.000	0.041	0.000
2	0.000	-0.051	0.000	-0.018
3	0.049	0.000	0.025	0.000
4	0.000	-0.011	0.000	-0.018

Table VI

Observed and Calculated Short-Range Order Parameters  $A_{\ell m}$   
for the Mo-21 and Mo-37 at .% Ta Alloys

$A_{\ell m}$	Mo-37 at .% Ta		Mo-21 at .% Ta	
	Observed	Calculated	Observed	Calculated
$A_{00}$	0.638	1.480	0.284	1.108
$A_{11}$	-0.356	-0.372	-0.190	-0.204
$A_{20}$	0.208	0.155	0.138	0.137
$A_{22}$	0.048	-0.040	0.051	0.045
$A_{31}$	-0.041	-0.054	-0.056	-0.074
$A_{33}$	0.001	0.020	-0.007	-0.026
$A_{40}$	0.026	-0.015	0.053	-0.025
$A_{42}$	-0.003	0.012	0.018	-0.050
$A_{44}$	-0.009	-0.026	0.004	-0.028

Table VII

Elastic Strain Terms  $L_{111}$  Derived from X-Ray Measurements

of Atomic Displacements Compared to Those Calculated

from Lattice Constants Assuming Hard Spheres

Atomic Pairs	Mo-21 at .% Ta		Mo-37 at .% Ta		Mo-91 at .% Ta	
	X-Ray	Hard Sphere	X-Ray	Hard Sphere	X-Ray	Hard Sphere
Mo-Mo	-0.0028	-0.0040	-0.0038	-0.0073		
Ta-Ta						0.0037
Mo-Ta		0.0101		0.0054		-0.010

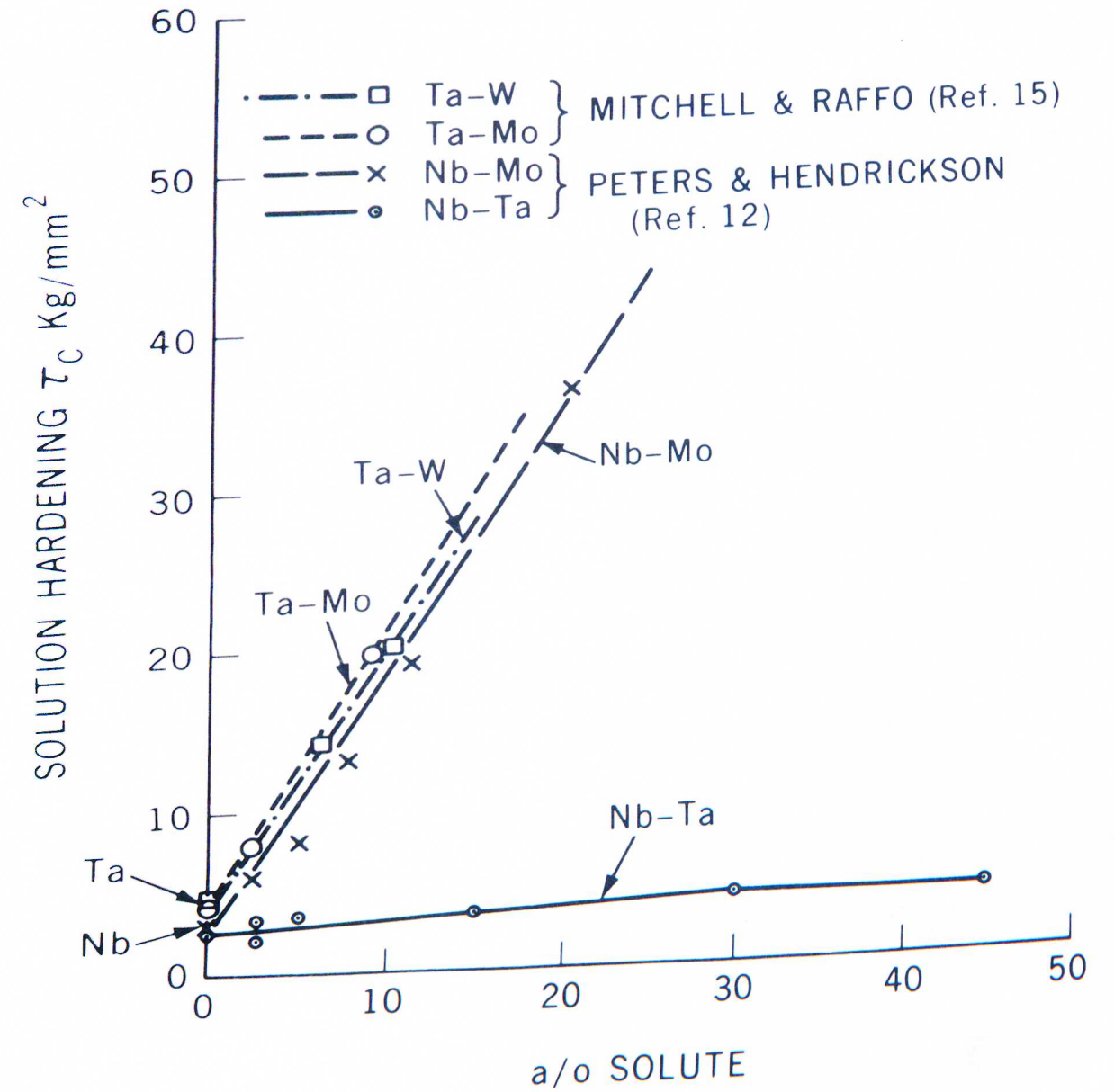


Figure 1. BCC Substitution Solid Solution Hardening of Ta and Nb at 300 K

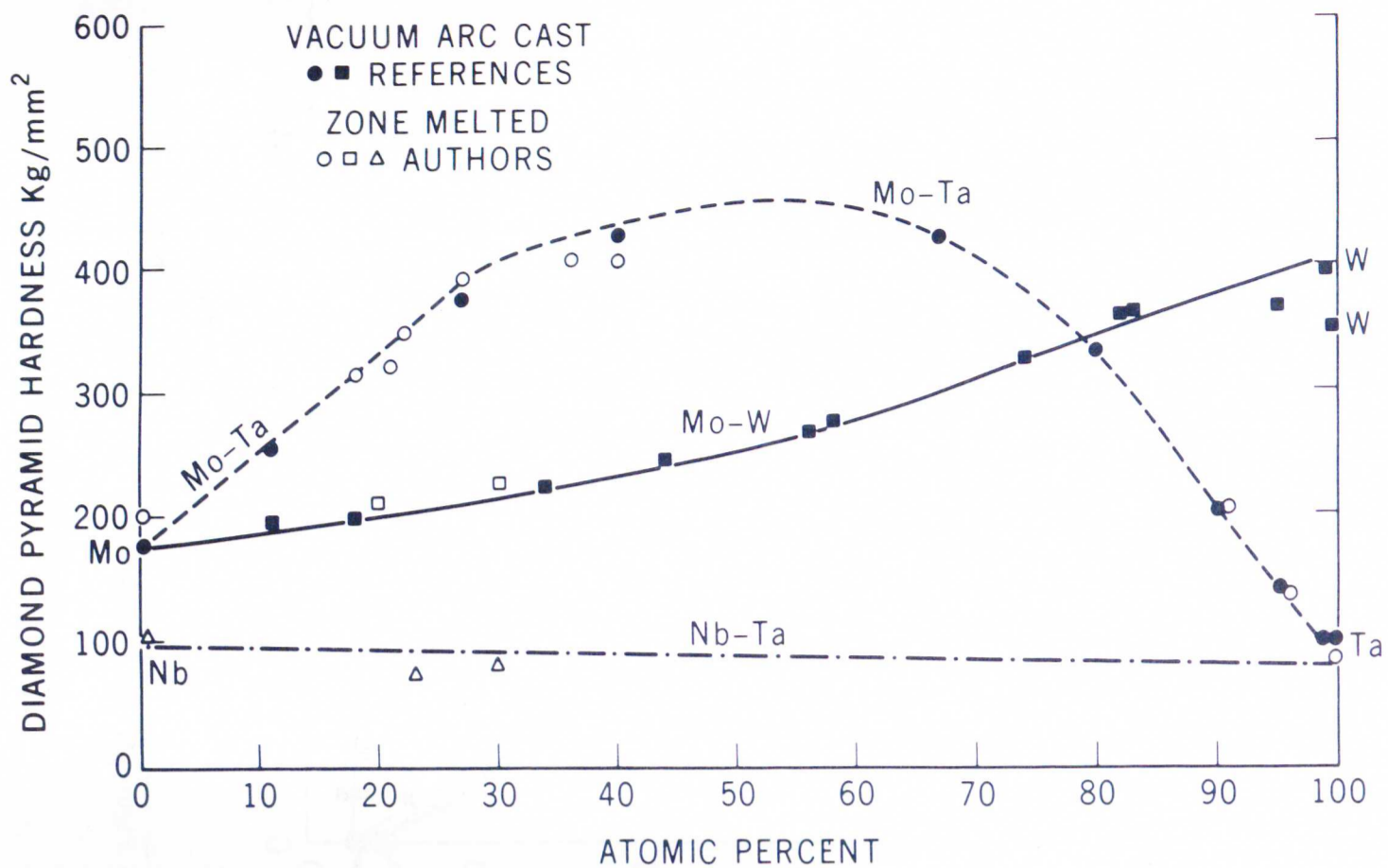


Figure 2. DPH Hardness of Binary Refractory Alloys at 300 K

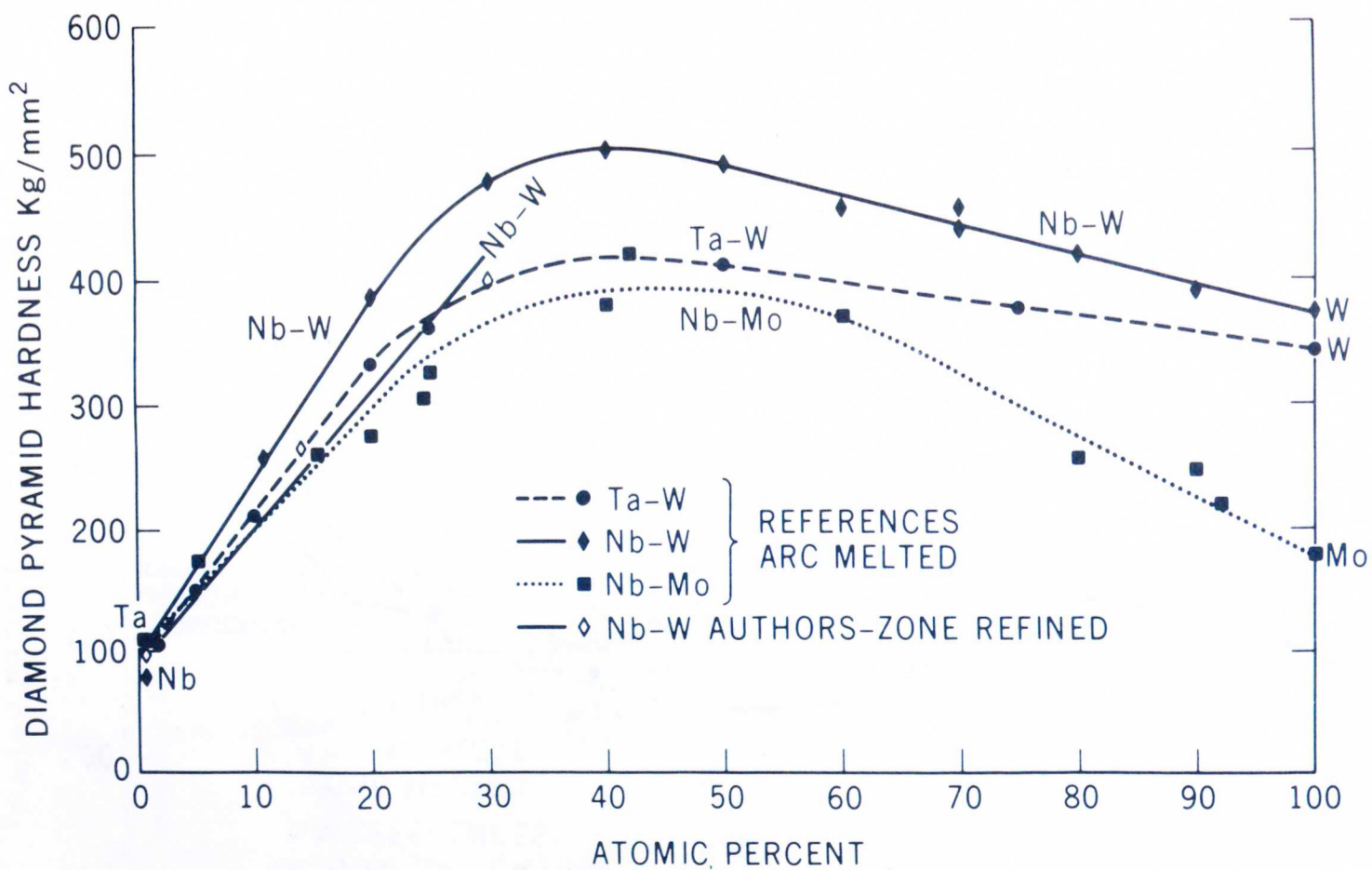


Figure 3. DPH Hardness of Binary Refractory Alloys at 300 K



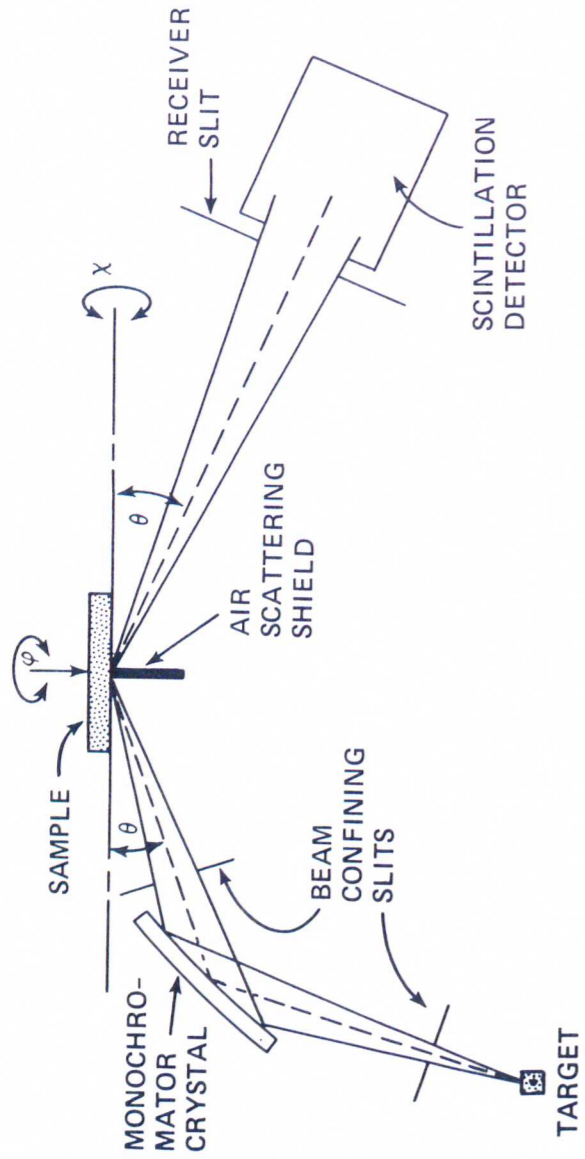


Figure 4. Schematic Representation of the Diffuse Scattering Geometry

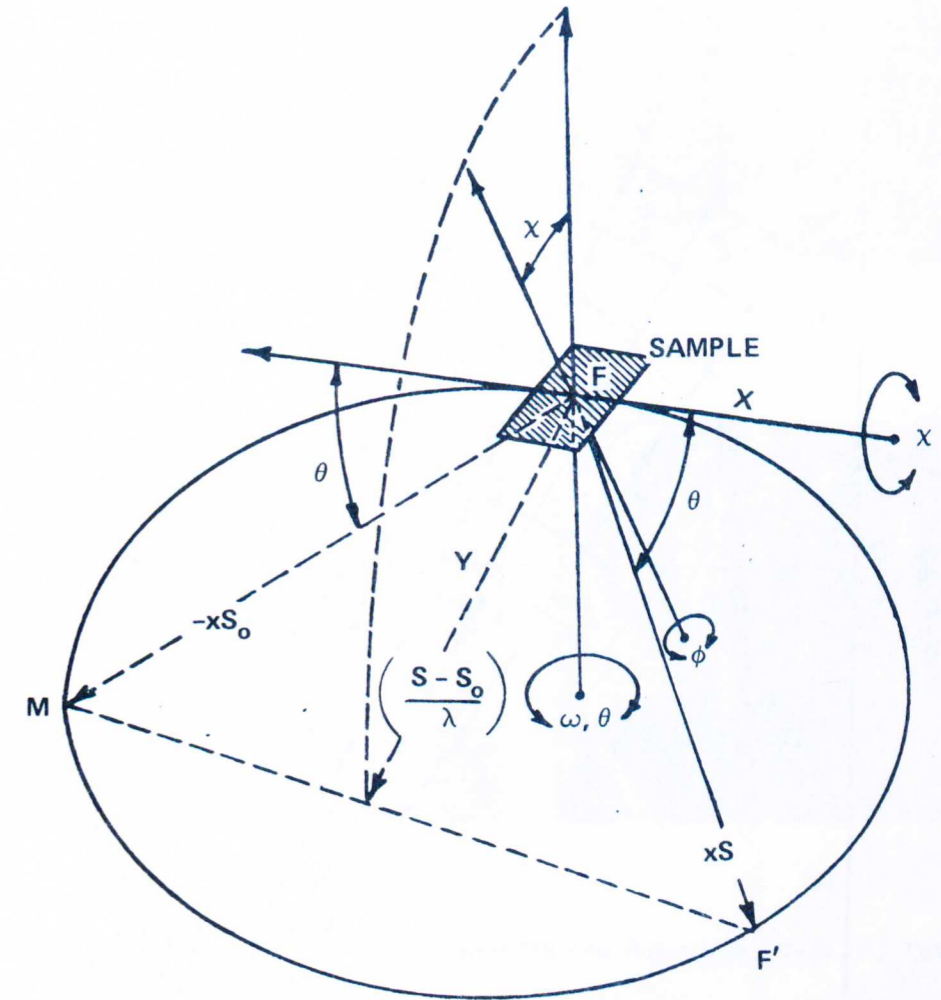


Figure 5. Geometry of the three-circle single-crystal diffractometer.

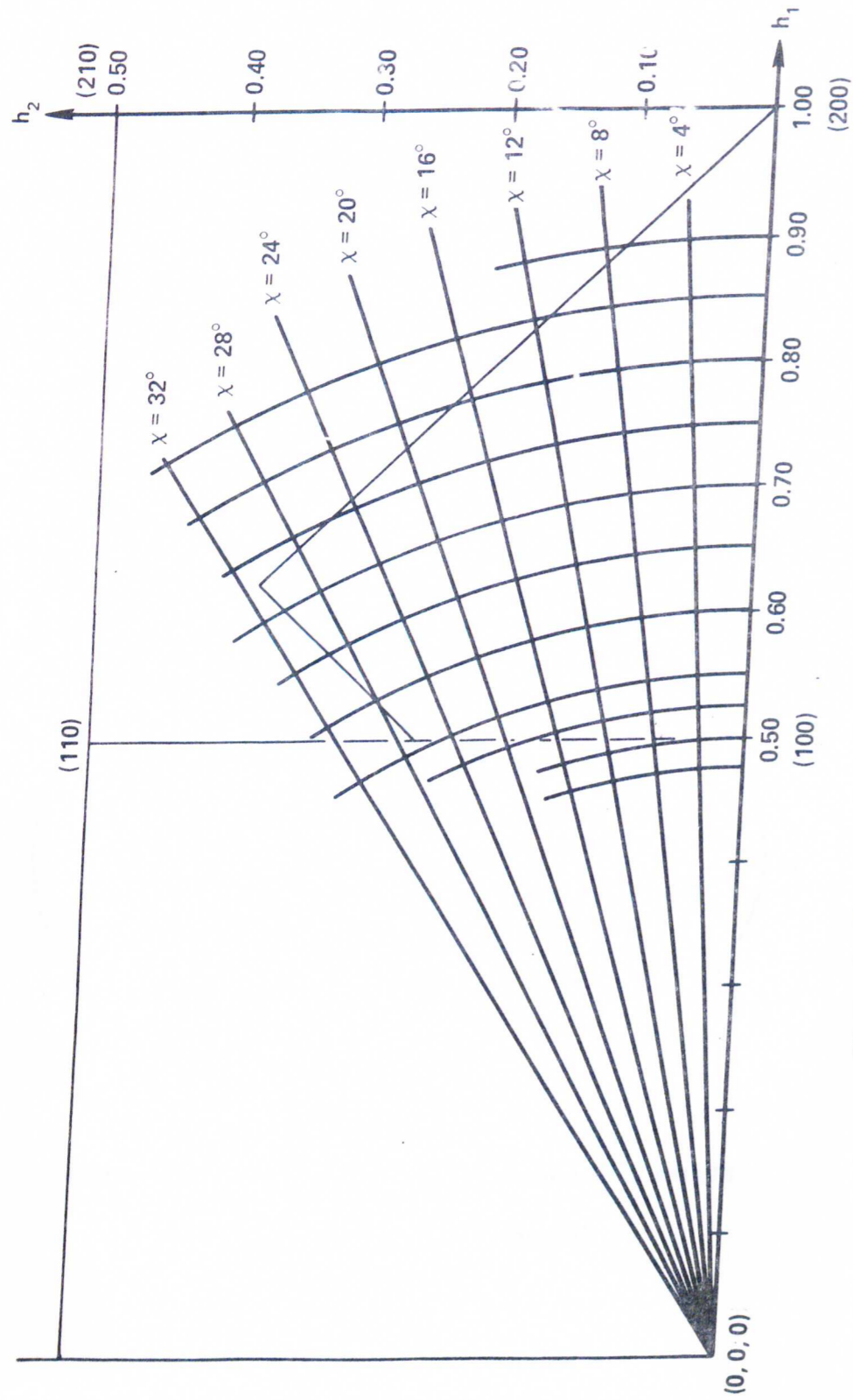


Figure 6. The Method of Scanning the Elementary Volume

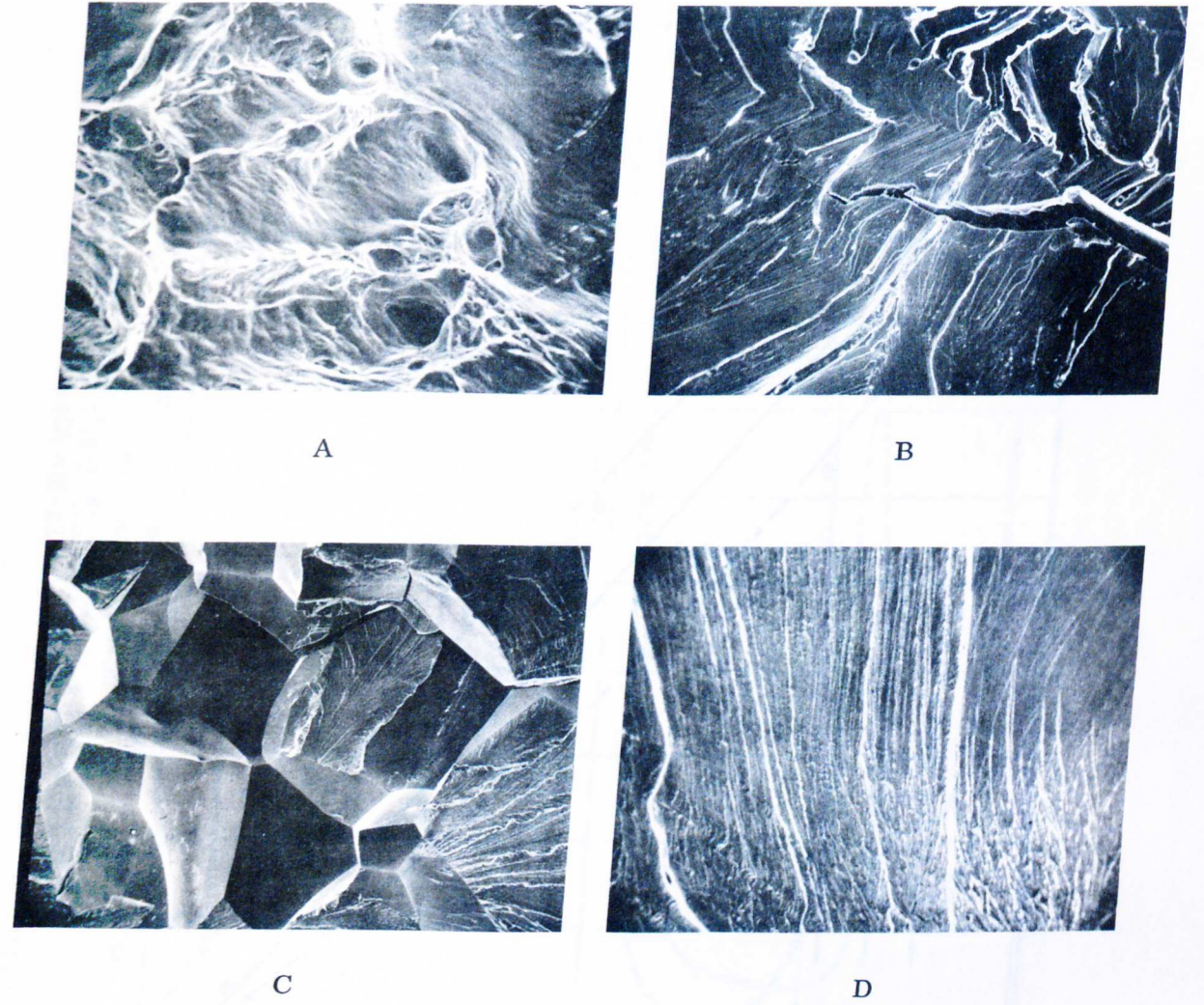


Figure 7. Fractographs of Refractory Binary Alloys at 300 K (A) Tearing and Cup-and-Cone fracture surface of the Ductile Ta-30 at .% Nb alloy (B) Cleavage fracture showing the river patterns for Mo-30 at .% W alloy (C) Intergranular fracture and cleavage fracture for polycrystalline Nb-14 at .% W (D) cleavage fracture for Ta-9 at .% Mo alloy.

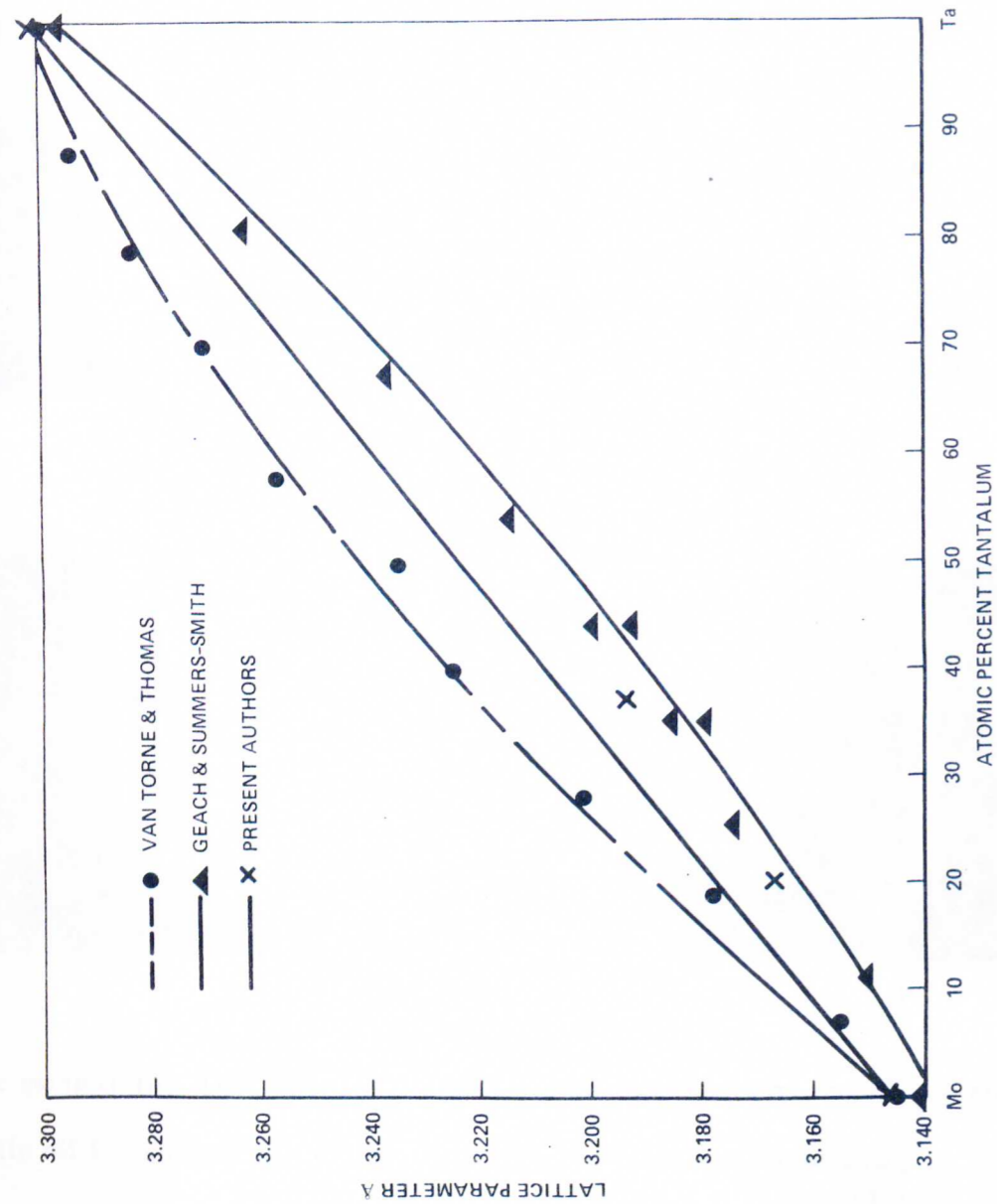


Figure 8. Lattice Parameters of Ta-Mo Alloys. Straight line

is a plot of Vegard's Law.

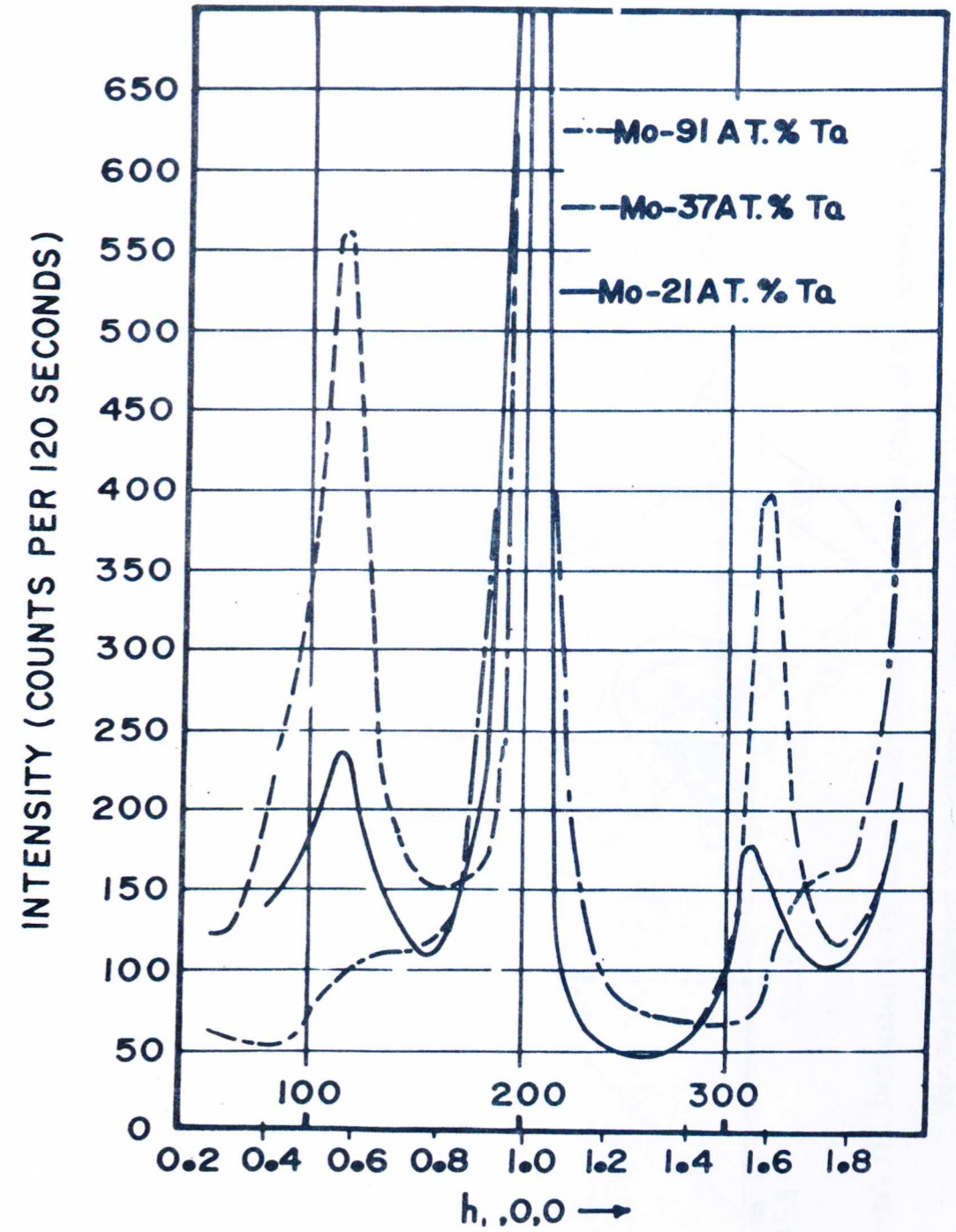


Figure 9. Diffracted Intensity Along  $(h_1, 0, 0)$  Axis in Reciprocal Space for Ta-Mo Alloys, Illustrating Asymmetry of the Short Range Order Peaks about (100) and (300) Positions.

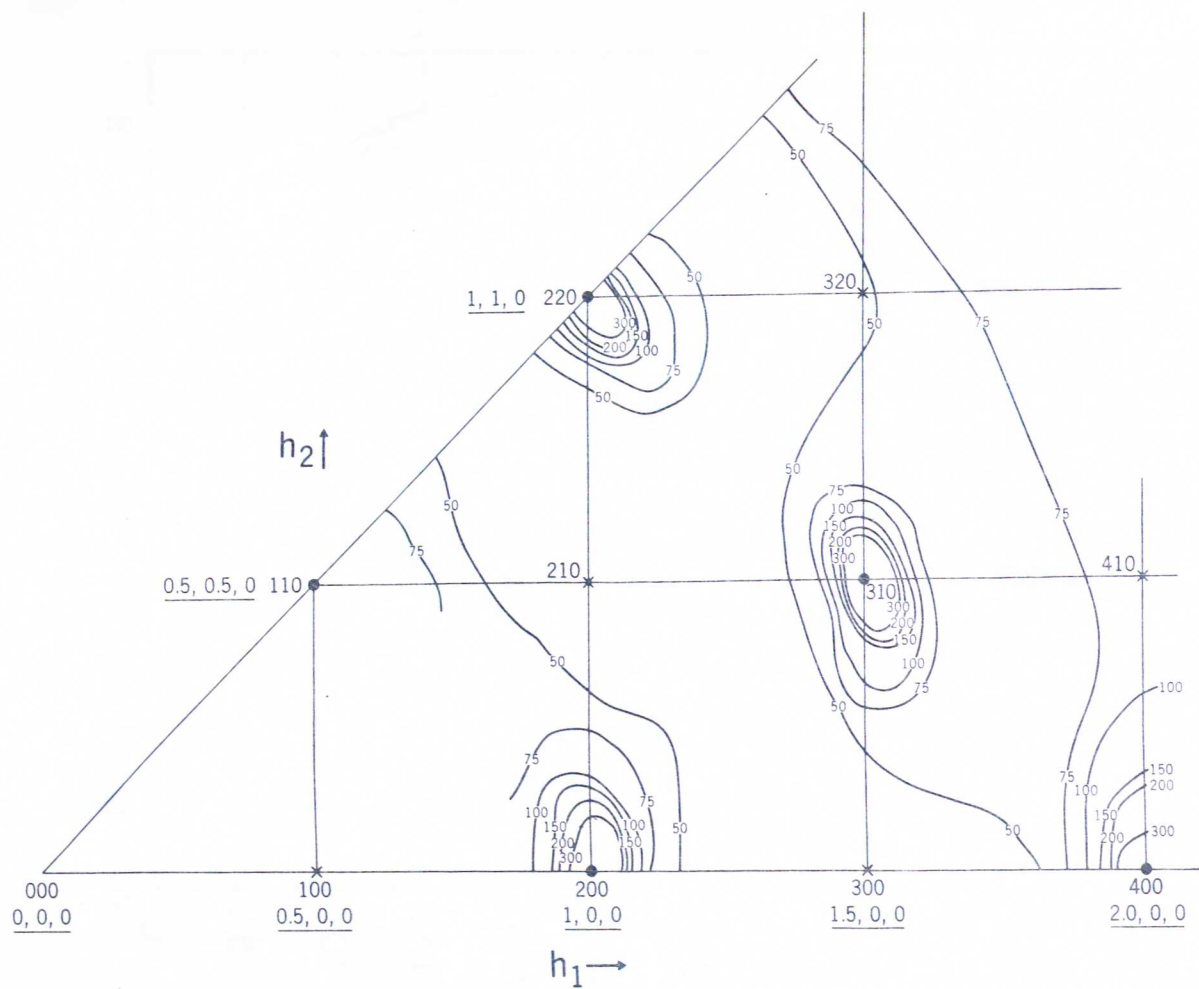


Figure 10. Diffracted X-Ray Intensity Distribution in the  $h_1 h_2 0$  Plane of Reciprocal Space for Mo at Ambient Temperature. Counts per 30 sec.

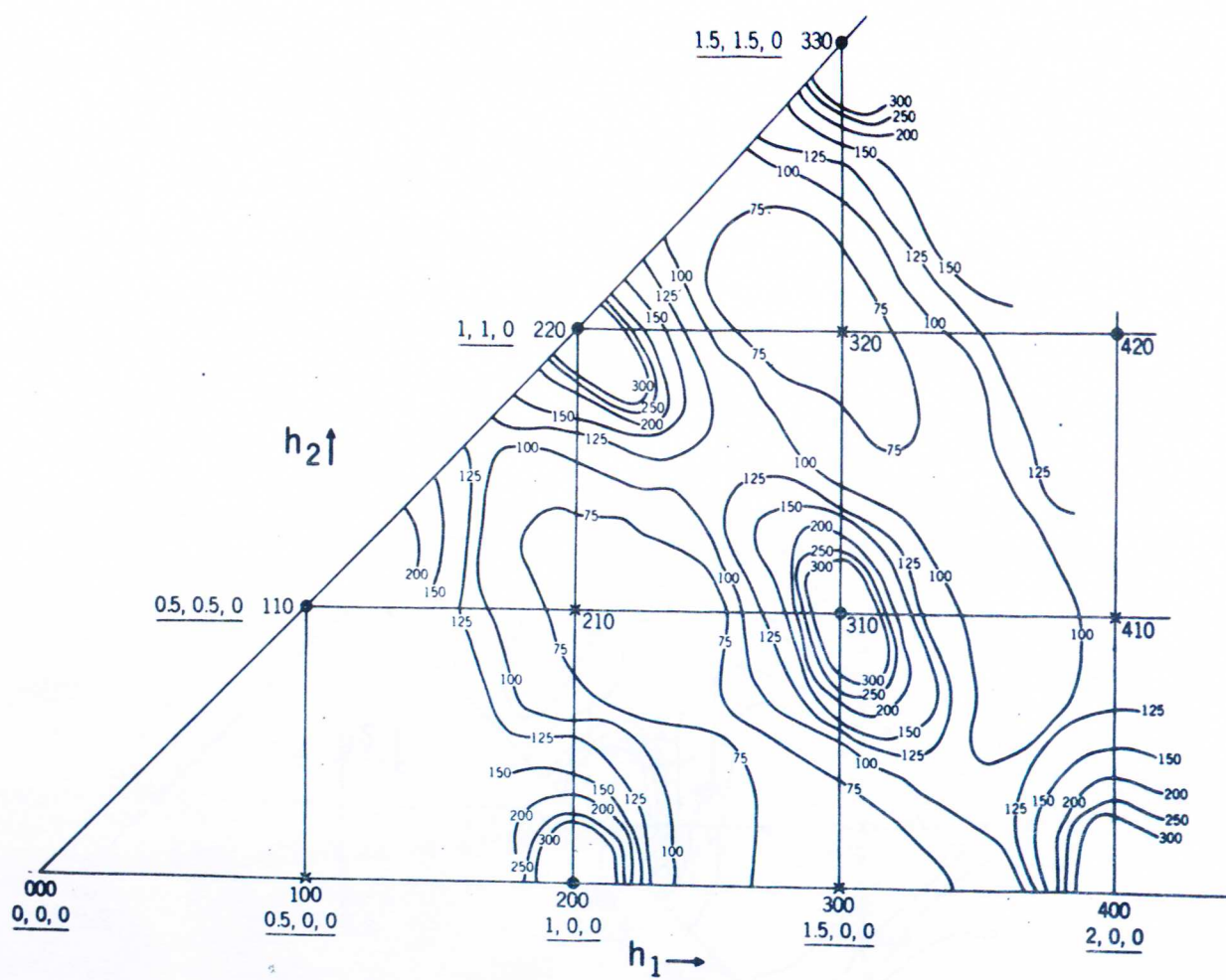


Figure 11. Diffracted X-Ray Intensity Distribution in the  $h_1 h_2 0$  Plane of Reciprocal Space for Ta at Ambient Temperature. Counts per 30 sec.

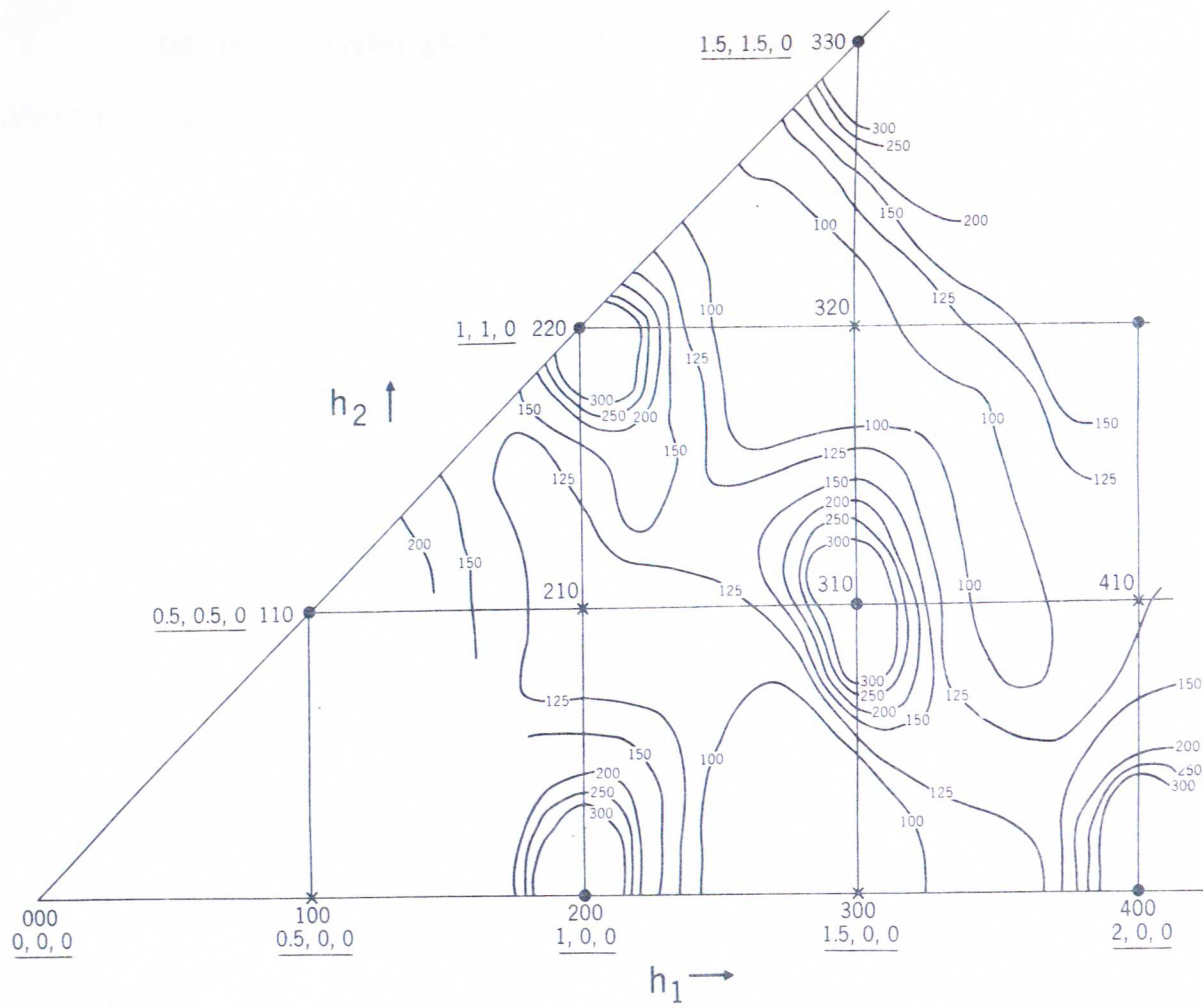


Figure 12. Diffracted X-Ray Distribution in the  $h_1 h_2 0$  Plane of Reciprocal Space for Nb-22% Ta at Ambient Temperature. X-Ray Intensity in Counts per 30 sec.

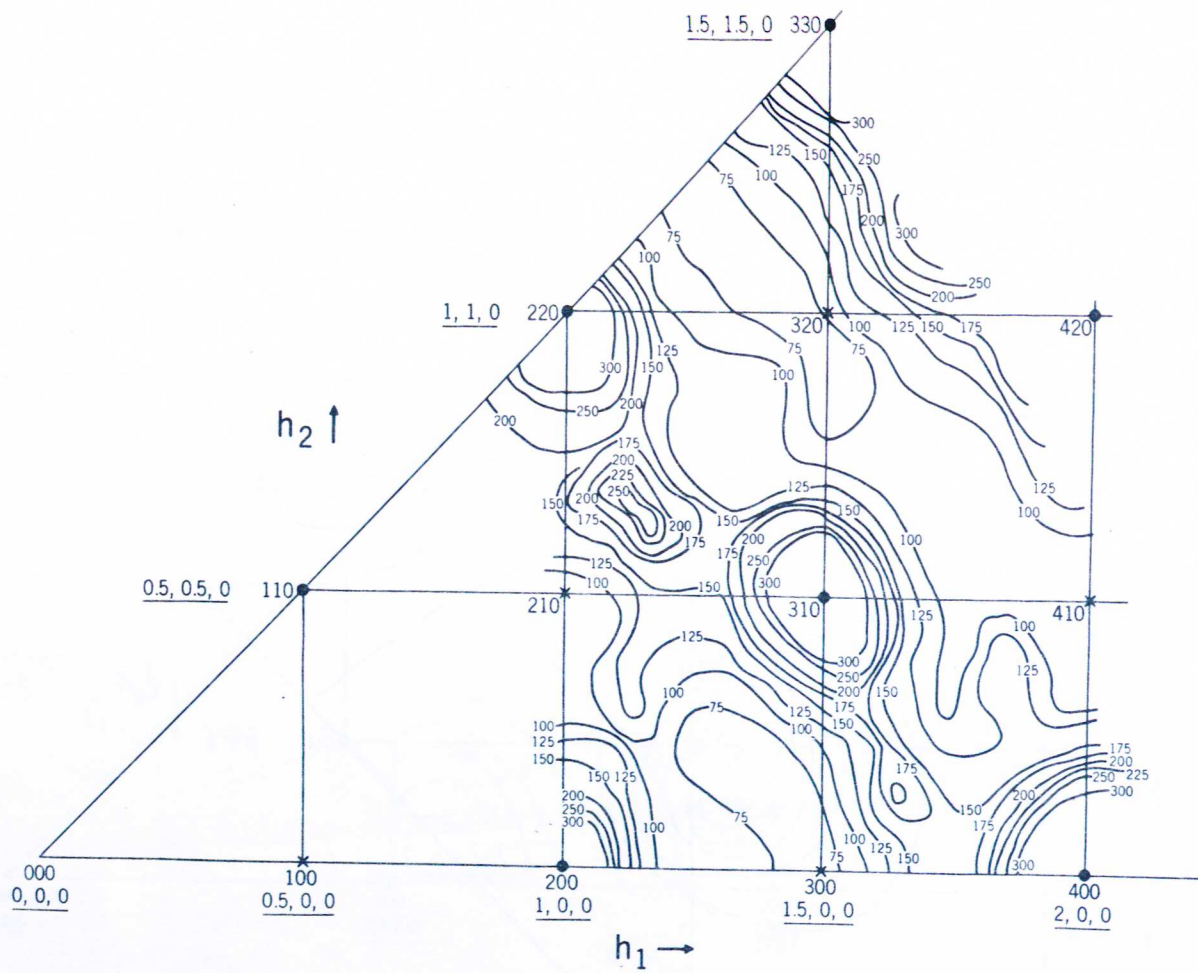


Figure 13. Diffracted X-Ray Intensity Distribution in the  $h_1 h_2 0$  Plane of Reciprocal Space for Mo-91% Ta at Ambient Temperature. X-Ray Intensity in Counts per 30 sec.

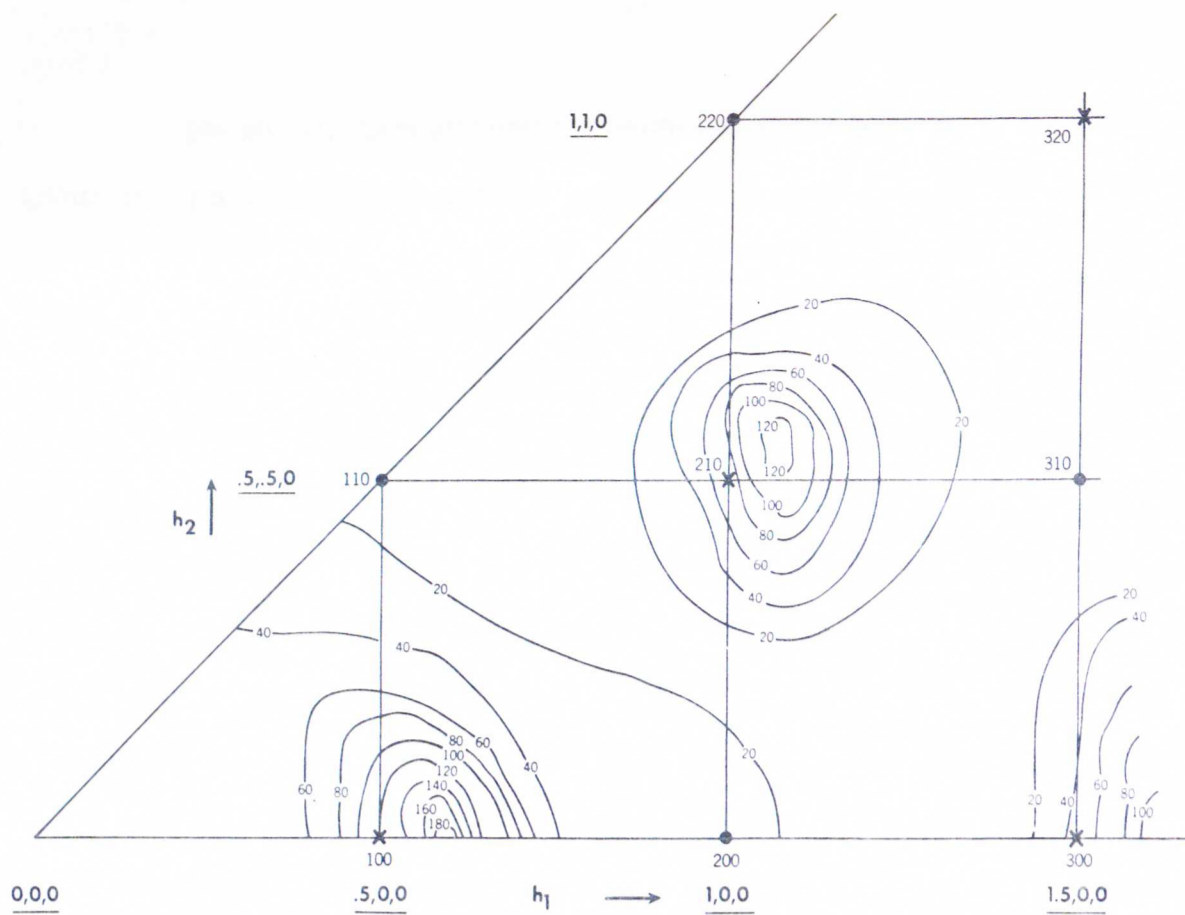


Figure 14. Diffuse Intensity Distribution in the  $h_1h_20$  Plane of Reciprocal Space for Mo-37% Ta at Ambient Temperature. Diffuse X-Ray Intensity in Counts per 60 sec.

62

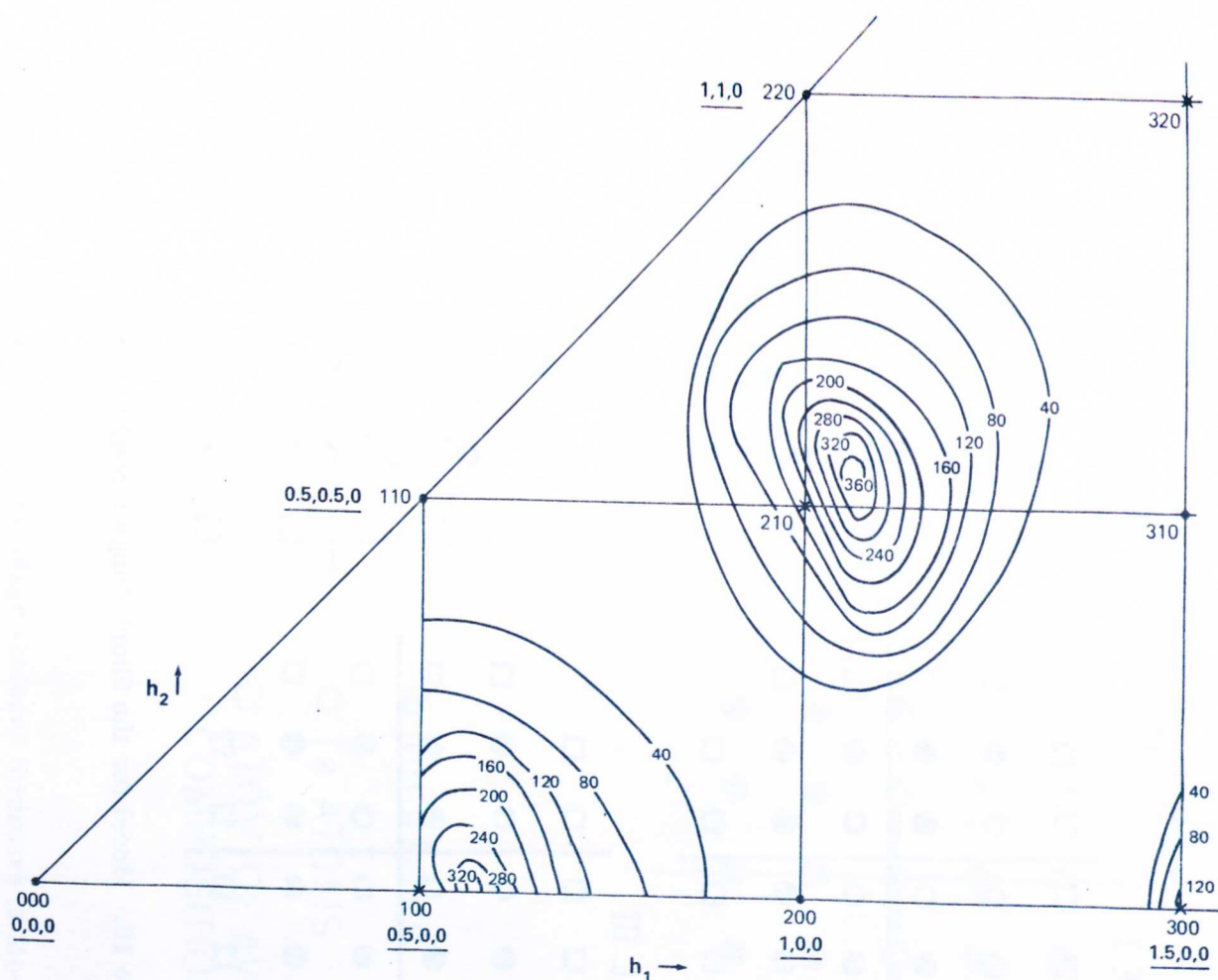


Figure 15. Diffuse Intensity Distribution in the  $h_1h_20$  Plane of Reciprocal Space for Mo-21 a/o Ta at Ambient Temperature. Diffuse X-Ray Intensity in Counts per 60 sec.

63

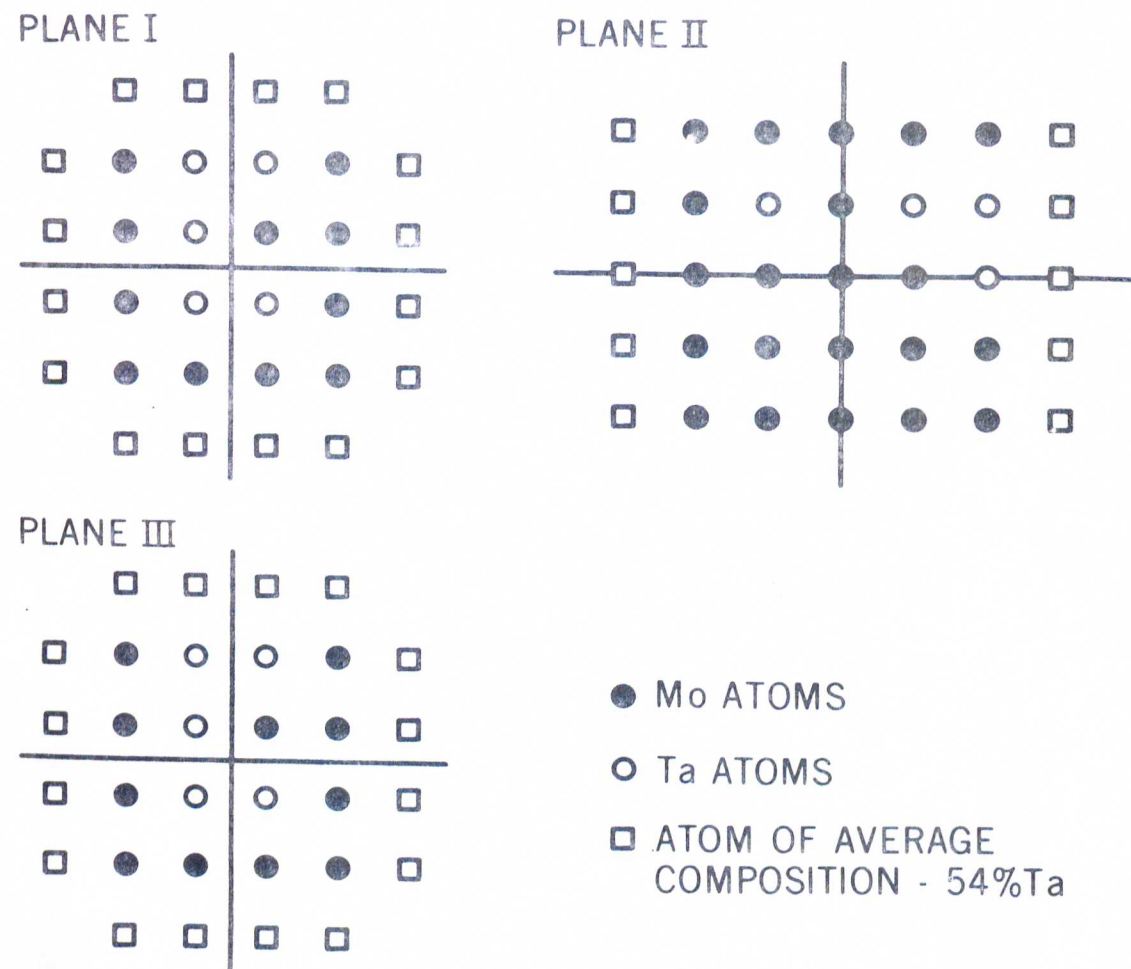


Figure 16. Model for the Short Range Ordered Structure of Mo-37 at .% Ta

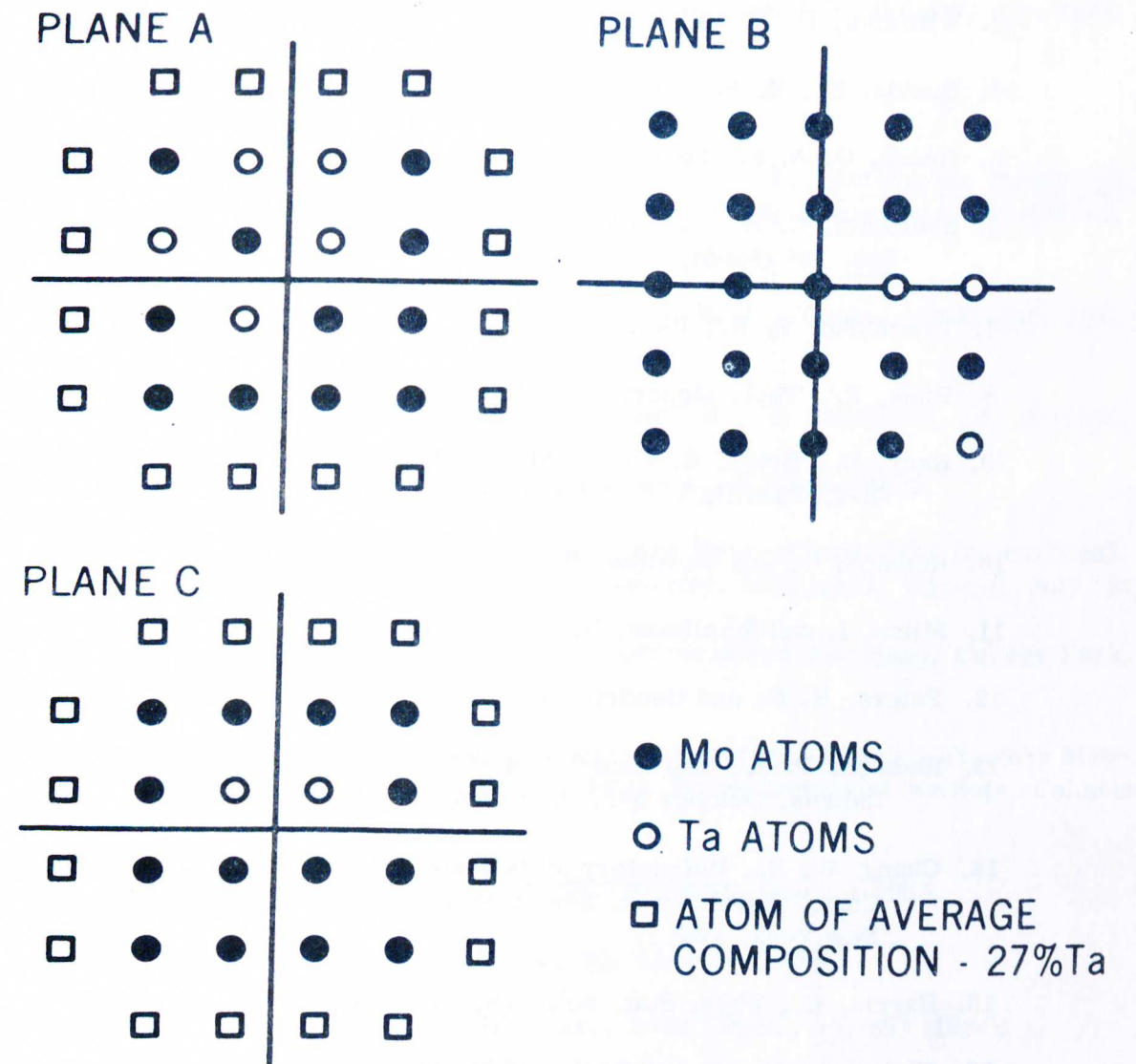


Figure 17. Model for the Short Range Ordered Structure of Mo-21 at .% Ta

## REFERENCES

1. Cowley, J. M., *J. Appl. Phys.*, 21, 24 (1950).
2. Warren, B. E., Averbach, B. L. and Roberts, S. W., *J. Appl. Phys.*, 22, 1493 (1951).
3. Williams, D. E. and Pechin, W. E., *Trans. ASM*, 50, 1081 (1958).
4. Buckle, H., *Z. Metallkde*, 37, 53 (1946).
5. Geach, G. A. and Summer-Smith, D., *J. Inst. Metals*, 80, 143 (1951-52).
6. Schramm, C. H., Gordon, P. and Kaufmann, A. R., *J. Metals*, New York, 188, 195 (1950).
7. Eremenko, V. H., *Ukr. Khim. Zh.*, 20, 227 (1954).
8. Rudy, E., Tech. Report No. AFML-TR-65-2, Part II, Vol. VIII (1966).
9. Rudy, E., Brukl, C. E. and St. Windisch, Tech. Report No. AFML-TR-65-2, Part II, Vol. XV and VII (1967).
10. Rudolph, G. and Mordike, B. L., *Z. Metallkde*, 58, 708 (1967).
11. Milne, I. and Smallman, R. E., *Trans. AIME*, 242, 120 (1968).
12. Peters, B. C. and Hendrickson, A. A., *Trans. AIME*, 1, 227 (1970).
13. Rudman, P. S., The Fourth Symposium on Refractory Metals, French Lick, Indiana, October 3-5, 1965, Gordon and Breach.
14. Chang, W. H., *Refractory Metals and Alloys*, Vol. 11, AIME Met. Soc. Conf., Edited by M. Semchysen and J. J. Harwood, Interscience, New York, 1961.
15. Harris, R., *Phys. Stat. Sol.*, 18, 715 (1966).
16. Fleischer, R., *Strengthening of Metals*, Edited by D. Peckner, p. 93, Reinhold, 1964.
17. Suzuki, H., *Nachr. Akad. Wiss. Göttingen, II., Math Phys. Kl.*, 1971, Nr. 6, p. 1-66.
18. Boser, O., *J. Appl. Phys.*, 44, 1038, (1973).
19. Harris, R., *Phys. Stat. Sol.*, 29, 383 (1968).
20. Foxall, R. A. and Statham, C. C., *Acta Met.*, 18, 1147 (1970).
21. Mitchell, T. E. and Raffo, P. L., *Canadian J. of Physics*, 45, 1047 (1967).
22. Das, G. E. and Arsenault, R. J., *Scripta Met.*, 2, 495 (1968).
23. Semchysen, M. and Barr, R. Q., *Refractory Metals and Alloys*, Edited by M. Semchysen and J. Harwood, Interscience Publishers, New York, 1961.
24. Meyers, R. H., *Metallurgica*, 42, 3 (1950).
25. Braun, H., Sedlatscheck, K. and Kieffer, B. F., *Columbium Metallurgy*, Edited by D. L. Douglass and F. W. Kunz, Interscience Publishers, New York, 1961.
26. Westgren, R. C., Kasak, A. and Dulis, E. J., *Trans. AIME*, 230, 1284 (1964).
27. Kieffer, R., Sedlatschek, K. and Braun, H., *Z. Metallkde*, 50, 18 (1959).
28. Singhal, S. C., Ph.D. Dissertation, Univ. of Penn., 1969.
29. Singhal, S. C. and Worrell, W. L., The Proceedings of the International Symposium of Metallurgical Chemistry, Middlesex, England, July 1971.
30. Beale, H. A., Ph.D. Dissertation, University of Maryland, College Park, Maryland, 1971.
31. Procedures for Metallographic Preparation of Be, Ti and Refractory Metals, DMIC Memo 37, October 26, 1959, Battle Memorial Institute, Columbus, Ohio.
32. Adler, I. and Goldstein, J., NASA TND 2984, October 1965.
33. Warren, B. E., *J. Appl. Phys.*, 25, 814-815 (1954).
34. Borie, B. S. and Sparks, C. J. Jr., *Acta Cryst.*, 17, 827 (1964).
35. Chipman, D. R., *Rev. Sci. Instr.*, 27, 164-165 (1956).
36. Sparks, C. J. and Borie, B. S., *Local Atomic Arrangements Studied by X-ray Diffraction*, Met. Society Conf. 36, Edited by J. B. Cohen and J. E. Hilliard, Gordon and Breach, New York, 1966.
37. Schwartz, L. H., Morrison, L. A. and Cohen, J. B., 7, 281-301, New York, Plenum Press, 1964.



38. Gilmore, C. J., Ph.D. Dissertation, University of Maryland, College Park, Maryland, 1971.
39. Metals Handbook, American Society for Metals, Metals Park, Ohio, 1961.
40. Rudman, P. S., *Acta Met.*, 12, 1381 (1964).
41. Borie, B. and Sparks, C. J., *Acta Cryst.*, 27, 198 (1971).
42. Epperson, J. E., Univ. of Tennessee, Dissertation, 1968.
43. Huang, K., *Proc. Roy. Soc. A*, 190, 102 (1947).
44. Wessel, E. T., France, L. L. and Begley, R. T., Columbium Metallurgy, Edited by D. L. Douglass and F. W. Kunz, Interscience, New York, 1961.
45. Raffo, P. L. and Mitchell, T. E., *Trans. AIME*, 242, 907 (1968).
46. Bechtold, J. H., Conference on Fracture, National Academy of Sciences, 1959.
47. Lement, B. S. and Kreder, K., Refractory Metals and Alloys IV, Edited by R. I. Jaffee, G. M. Ault, J. Maltz and M. Semchysen, Gordon and Breach, New York, N.Y., 1967.
48. Wilcox, B. A. and Gilbert, A., Refractory Metals and Alloys IV, Edited by R. I. Jaffee, G. M. Ault, J. Maltz and M. Semchysen, Gordon and Breach, 1967.
49. Beardmore, P. and Hull, D., Refractory Metals and Alloys IV, Edited by R. I. Jaffee, G. M. Ault, J. Maltz and M. Semchysen, Gordon and Breach, 1967.
50. Beardmore, P. and Hull, D., *J. Less-Common Metals*, 9, 168 (1965).
51. Wronski, A. and Fourdeux, A., *J. Less-Common Metals*, 8, 149 (1965).
52. Gilbert, A., *J. Less-Common Metals*, 10, 328 (1966).
53. Forster, R. H. and Gilbert, A., *J. Less-Common Metals*, 20, 315 (1970).
54. Ferriss, D. P., Rose, R. M. and Wulff, J., *Trans. AIME*, 224, 584 (1962).
55. Van Torne, L. I. and Thomas, G., *Acta. Met.*, 14, 621 (1966).
56. Warren, B. E. and Averbach, B. L., Modern Research Techniques in Physical Metallurgy, ASM, Cleveland, 1953.

57. Walker, C. B. and Keating, D. T., *Acta. Cryst.*, 14, 1170 (1961).
58. Cromer, D. T., *J. Chem. Physics*, 50, 4857 (1969).
59. Cromer, D. T. and Mann, J. B., *J. Chem. Phys.*, 47, 1892 (1967).
60. Epperson, J. E. and Spruiell, J. E., *J. Phys. Chem. Solids*, 30, 1733 (1969).
61. Labusch, R., *Phys. Stat. Sol.*, 41, 659 (1970).
62. Mott, N. H. and Nabarro, F. R. N., *Strength of Crystals*, Phys. Soc., London, 1948.
63. Riddhaghi, B. R. and Asimow, R. M., *J. Appl. Phys.*, 39, 4144 (1968).
64. Riddhaghi, B. R. and Asimow, R. M., *J. Appl. Phys.*, 39, 5169 (1968).
65. Foreman, A. J. E. and Makin, J. J., *Phil. Mag.*, 14, 911 (1966).
66. Friedel, J., *Dislocations*, Addison-Wesley Pub. Co., Reading, 1964.
67. Flinn, P. A., *Acta. Met.*, 6, 631 (1958).
68. Eshelby, J. D., *Solid State Physics Volume 3*, Edited by F. Seitz and D. Turnbull, Academic Press Inc., New York, 1956.
69. Hobson, D. O., Oak Ridge National Laboratory Report, ORNL-3678, 1964.
70. Dugdale, D. S., *J. of Mech. and Phys. of Solids*, 6, 85 (1958).
71. Tabor, D., *Hardness of Metals*, Clarendon Press, Oxford, 1951.
72. Hasson, D. F., Huang, Y., Pink, E., Arsenault, R. J., *Met. Trans.*, 5, 371 (1974).
73. Armstrong, R. W., *J. of Sci. and Ind. Res.*, 32, 591 (1973).
74. Arsenault, R. J., *Acta. Met.*, 17, 1291 (1969).
75. Armstrong, D. A., Mordike, B. L., *Z. Metallkde*, 61, 356 (1970).
76. Walker, C. B. and Keating, D. T., *Phys. Rev.* 130, 1726 (1963).
77. Averbach, B. L., *Energetics in Metallurgical Phenomena*, Edited by W. M. Mueller, Gordon and Breach, New York, 1965.

## LIST OF SYMBOLS

$\tau^*$	effective stress or thermal component of yield of stress
$\tau\mu$	athermal component of yield stress
$T_c$	temperature at which $\tau^*$ is zero
$X$	diffraction coordinate
$\varphi$	diffraction coordinate
$\omega$	diffraction coordinate
$2\theta$	scattering angle
$X$	diffraction coordinate
$Y$	diffraction coordinate
$\lambda$	x-ray wavelength
$I_{ORDER+AD}$	component of diffracted intensity due to order and atomic displacement
$I_{F+S}$	component of diffracted intensity due to fluorescence and submultiple wavelength components
$I_C$	component of diffracted intensity due to incoherent scattering
$I_{TDS}$	component of diffracted intensity due to temperature diffuse scattering from the sample
$I_{FUND}$	component of diffracted intensity due to sharp fundamental Bragg reflections
$I_{HUANG}$	component of diffracted intensity due to Huang diffuse scattering
$I_{eu}$	intensity in electron units
$f_p, f_q$	scattering factors of atoms situated on sites p and q
$K$	$\frac{2\pi}{\lambda} (\hat{S} - \hat{S}_0)$
$R_{pq}$	interatomic vector
$h_1, h_2, h_3$	continuous rectangular coordinates in reciprocal space
$N$	total number of atoms being irradiated by the x-ray beam
$X_A, X_B$	mole fractions of element A and B
$f_A, f_B$	scattering factors for elements A and B
$\ell, m, n$	discrete variables specifying an atom's position relative to the origin
$\alpha_{\ell mn}$	Warren order parameters
$\langle \delta^2 \rangle_{\ell mn}^{\ell}, \langle \delta^2 \rangle_{\ell mn}^m$	mean square atomic displacement parameters

$\langle \delta \rangle_{\ell mn}^{\ell m}, \langle \delta \rangle_{\ell mn}^{A A}$	mean square cross atomic displacement parameters
$\langle \delta \rangle_{\ell mn}^{B A}, \langle \delta \rangle_{\ell mn}^{B B}$	
$a_1, a_2, a_3$	translational vectors of a cubic unit cell
$b_1, b_2, b_3$	base vectors reciprocal to $\frac{a_1}{2}, \frac{a_2}{2}$ and $\frac{a_3}{2}$
$\hat{S}, \hat{S}_0$	unit vectors specifying the direction of the scattered and incident beams, respectively
$P_{\ell mn}^{B A}$	conditional probability of finding an A atom at the site p if there is an atom at site q
$\gamma_{\ell mn}^{\ell}$	three dimensional first-order size-effect parameters
$L_{\ell mn}^{A A}, L_{\ell mn}^{A B}, L_{\ell mn}^{B B}$	components of the displacement of an atom off the average lattice site parallel to $\frac{a_1}{2}, \frac{a_2}{2}$ and $\frac{a_3}{2}$ respectively.
$A_{\ell m}$	two dimensional Warren order parameters
$\Gamma_{mn}^{\ell}$	two dimensional first order size-effect parameters

VITA

Name: Roamer Edward Predmore

Permanent Address: 14003 Flint Rock Road  
Rockville, Maryland 20853

Degree and Date to be Conferred: Ph.D., 1975

Date of Birth: August 10, 1937

Place of Birth: Detroit, Michigan

Secondary Education: Caro High School, 1956, Caro, Michigan

Collegiate Institutions Attended:	Dates	Degree	Date of Degree
Michigan Technological University	1956-60	B. Met. Eng. (cum laud)	1960
Northwestern University	1960-60	—	—
Catholic University of America	1962-64	M. S. (Eng.)	1964
University of Maryland	1964-75	Ph.D.	1975

Major: Engineering Materials

Minor: Chemical Engineering, Mechanical Engineering

Publications:

1. R. E. Predmore, S. Ahmed and R. Kumar, "Predictions of Solar Induced Response of Thin-Walled Open-Section Booms for Design." Proceedings of the International Symposium on Experimental Mechanics, University of Waterloo, Waterloo, Ontario, Canada, June, 1972.
2. R. E. Predmore, R. J. Arsenault and C. J. Sparks, Jr., "Strengthening and Fracture of Ta, Nb, Mo and W. Binary Solid Solutions with Short Range Order" Proceedings of the International Conference on Mechanical Behavior of Materials, Kyoto, Japan, 1971.
3. R. E. Predmore, R. J. Arsenault, and C. J. Sparks, Jr., "Local Atomic Arrangements in Ta-Mo and Ta-Nb B.C.C. Alloys."

VITA - Continued

- Proceedings of the Seminar on Metals, August, 1971, Tokyo, Japan,  
The Society of Materials Science, Japan, Ed. S. Taira.
4. R. E. Predmore "Experimental Thermal Mechanics of Deployable Boom Structures" Significant Accomplishments in Technology, 1970, National Aeronautics and Space Administration, Washington, D.C. 1972.
  5. R. E. Predmore, J. Jellison and C. L. Staugaitis, "Friction and Wear of Steels in Air and Vacuum" ASLE TRANS. 14, 23 (1971).
  6. R. E. Predmore and R. J. Arsenault "Short Range Order of Ta-Mo Alloys" Scripta Met. 4, 213 (1970) .
  7. R. E. Predmore and E. P. Klier "Martensite Start Temperatures Versus Pressure for 43XX Steels" Transactions of ASM 62, 768 (1969).
  8. J. Jellison, R. E. Predmore, C. L. Staugaitis "Sliding Friction of Copper Alloys in Vacuum" ASLE Transactions 12, 771 (1969).
  9. H. E. Frankel, A. J. Babecki and R. E. Predmore, "Some Considerations of Advanced Welding Technology" British Welding Journal April (1966) 189.